Stealth export of hydrogen and methane from a low temperature serpentinization system

Larson B.I.[a,b] Lang S.Q.[c], Lilley M.D.[a], Olson E.J.[a], Lupton J.[d], Nakamura K.[e], Buck N.J.[b]

[a]School of Oceanography, University of Washington, Seattle, WA 98105
[b]JISAO / PMEL, University of Washington, Seattle, WA 98115
[c]Department of Earth and Ocean Sciences, University of South Carolina, Columbia, SC 29208
[d]NOAA / PMEL, Hatfield Marine Science Center, Newport, OR 97365
[e]National Institute of Advanced Industrial Science and Technology, Tsukuba, Ibaraki 305-8567, Japan

INSERT KEYWORDS

ABSTRACT

Chemical input to the deep sea from hydrothermal systems is a globally distributed phenomenon. Hydrothermal discharge is one of the primary mechanisms by which the Earth's interior processes manifest themselves at the Earth's surface, and it provides a source of energy for autotrophic processes by microbes that are too deep to capitalize on sunlight. Much is known about the water column signature of this discharge from high temperature mid-ocean Ridge (MOR) environments and their neighboring low-temperature counterparts. Hydrothermal discharge farther away from the ridge, however, has garnered less attention, owing in part to the difficulty in finding this style of venting, which eludes methods of detection that work well for high-temperature 'black smoker' type venting. Here we present a case study of the plume from one such 'invisible' off-axis environment, The Lost City, with an emphasis on the dissolved volatile content of the hydrothermal plume. Serpentinization and abiotic organic synthesis generate significant concentrations of H_2 and CH_4 in vent fluid, but these species are unevenly transported to the overlying plume, which itself appears to be a composite of two different sources. A concentrated vent cluster on the talus slope channels fluid through at least 8 chimneys, producing a water column plume with the highest observed concentrations of CH_4 in the field. In contrast, a saddle in the topography leading up to a carbonate cap hosts broadly distributed, nearly invisible venting apparent only in its water column signals of redox potential and dissolved gas content, including the highest observed plume H_2. After normalizing H_2 and CH_4 to the ^3He background-corrected anomaly ($^3He^{\Delta}$) to account for mixing and relative amount of mantle input, it appears that, while a minimum of 60% of CH_4 is transported out of the system, greater than 90% of the H_2 is consumed in the subsurface prior to venting. The exception to this pattern occurs in the plume originating from the area dubbed Chaff Beach in which somewhat more than 10% of the original H_2 remains, indicating that this otherwise unremarkable plume, and others like it, may represent a significant source of H_2 to the deep sea.

1. Introduction

The Lost City field is a manifestation of low temperature (<250°C) circulation through ultramafic rocks and remains, thus far, a unique oceanographic expression of serpentinization related venting. The field features up to 60 m high carbonate edifices that vent < 91°C, pH 9-11, metal-poor fluids (Kelley et al., 2001, 2005; Früh-Green et al., 2003; Ludwig et al., 2006). Fluid-rock reactions in the underlying ultramafic rocks result in highly reducing fluids with milli-molar concentrations of hydrogen (H_2). Fluids also contain high concentrations of methane (CH_4), C_2^+ alkanes, and formate, whose formation has been attributed to abiological synthesis based on their relative concentrations, stable isotopes (^{13}C, ^{2}H), and radiocarbon content (Proskurowski et al., 2008; Lang et al., 2010). The porous carbonate chimneys are dominated by novel CH_4-cycling archaea (Schrenk et al., 2004). Similar low temperature water-rock reactions are increasingly being identified in continental systems, where the physical manifestations in the form of large travertine deposits and alkaline springs are more readily observed. High pH springs have now been identified in Oman, California, Italy, Newfoundland, New Caledonia, Yougoslavia, Turkey, and the Philippines (Barnes et al., 1978; Neal and Stanger, 1983; Abrajoano et al., 1988, 1990; Fritz et al., 1992; Cipolli et al., 2004; Hosgormez et al., 2008; Marques et al., 2008; Blank et al., 2009; Etiopeet et al., 2011; Schwarzenbach et al., 2013; Szponar et al., 2012).

The high concentrations of CH_4 and H_2 derived from the serpentinization of ultramafic rocks result in large export fluxes to the deep sea in amounts far greater than that from basalt-hosted systems (Cannat et al., 2010; Charlou et al., 2010; Keir, 2010). Approximately 70% of the total mid-ocean flux of these gases is due to serpentinite-hosted water-rock interactions, despite the fact that the total subsurface water flow through these systems is significantly smaller (~8%; Keir, 2010). The majority of identified systems impacted by serpentinization, such as Rainbow and Logatchev, are high temperature (>350°C) and share some features with basalt hosted hydrothermal systems such as low pHs and fluids rich in iron and manganese (Charlou et al., 2010). The concentrations of CH_4 and H_2 in endmember vent fluids from Lost City are similar to those of Rainbow and Logatchev but, due to the lower exit temperatures, the CH_4/heat and H_2/heat ratios are ~3-7 times higher (Cannat et al., 2010).

Low temperature serpentinization systems are expected to occur in other oceanographic locations where ultramafic rocks are exposed to seawater, but other such systems have eluded detection. One possible exception is the extinct 'Ghost City,' adjacent to the high temperature Rainbow field, where carbonate chimneys may be indicative of a formerly active low temperature, high pH type of system (Lartaud et al., 2011).

It is possible that Lost City type circulation is unique, making such an environment relatively unimportant in terms of chemical fluxes to the deep sea. Given the high incidence of similar continental springs, as well as the wide exposure of ultramafic rocks on the seafloor, this seems unlikely however. Instead, such circulation may be widespread but undiscovered. Most

oceanographic hydrothermal fields are identified by instrument packages towed by surface ships. Warm fluids rise buoyantly and mix with deep seawater, and the resulting plume has diagnostic characteristics that can be detected such as small increases in temperature or suspended particulates due to the precipitation of metal rich particles in the water column (German and Von Damm, 2003). Vent fluids from Lost City, however, are of lower temperature (≤91°C) than those from most magmatically driven systems (>300°C), and lack the significant concentrations of dissolved iron and manganese that would lead to particle formation (Kelley et al., 2005). Lost City type hydrothermal systems will therefore be difficult to detect by traditional methods.

The relative fate of reduced chemical species such as CH_4 and H_2 has implications for fluxes to the deep sea from systems typified by the Lost City field, and for the microbial communities that utilize these reduced compounds as a source of energy or carbon. Within the endmember fluids of the Lost City field itself, hydrogen concentrations vary widely (0.5 – 14 mM) and are believed to support subsurface microbial sulfate reduction (Proskurowski et al., 2006; Lang et al., 2012). In contrast, much smaller concentration differences in methane (1 – 2 mM) are strongly associated with the relative amount of mantle input, as identified by concentrations of ^3He (Proskurowski et al., 2008).

The goals of this work are two-fold: (1) to characterize the water column features of this particular system as an aid to future exploration for similar systems; and (2) to identify the fate of the reduced volatiles H_2 and CH_4 as vent fluids mix with oxygenated seawater, particularly in relation to subsurface processes. During a 2003 cruise to the Lost City field, we used 14 vertical hydrocasts to characterize the plume over the Lost City field. We report here on the water column characteristics of serpentinization-related venting including potential temperature, turbidity, Eh, and concentrations of CH_4, H_2, and helium (He).

2. Background

2.1. Geological Setting

Geologic investigations of the Atlantis Massif ocean core complex resulted in the serendipitous discovery of large carbonate-brucite towers and the Lost City hydrothermal field in December 2000 (Kelley et al., 2001). The ~3800 m high seamount is located at 30°N, on the inside corner high of the Mid-Atlantic Ridge and the Atlantis transform fault. It is composed of ~1-2 Myr-old ultramafic rocks with lesser gabbro that have been exposed by long-lived detachment faulting (Kelley et al., 2001; Blackman et al., 2002; Früh-Green et al., 2003; Karson et al., 2006; Boschi et al., 2008).

The field rests on a down-dropped terrace at a water depth of 750-850 m; active venting is found along a broadly linear east-west zone, with 8 identified locations where fluids are focused through large, up to 60 m high, carbonate-brucite chimneys (Fig. 1; Kelley et al., 2001;

2005; Früh-Green et al., 2003; Karson et al., 2006). The top of the massif is capped by a ~1 m thick layer of carbonate ooze that has been hydrothermally-cemented (Kelley et al., 2001; 2005; Blackman et al., 2002; Früh-Green et al., 2003; Karson et al., 2006). Radiocarbon and U-Th dating of the carbonate chimneys indicates the field has been present for up to 120 kyr (Früh-Green et al., 2003; Ludwig et al., 2011).

2.2. Vent Sites

The chimneys at the center of the Lost City field (Fig. 1) are hotter and have fluids with higher hydrogen concentrations than those at the periphery of the field (Proskurowski et al., 2006). The decrease in hydrogen concentrations, from 14 to 0.5 mmol/kg, corresponds with a decrease in sulfate and an increase in sulfide concentrations in the ratio expected for microbial sulfate reduction (Proskurowski et al., 2006; Lang et al., 2012). Chimneys on the outer rim of the field, are at greater water depths, and host lower-temperature fluids with lower hydrogen concentrations (Proskurowski et al., 2006).

3. Methods

Following the initial discovery of the Lost City hydrothermal field in 2000, a research cruise was undertaken in 2003 to characterize the field using the manned submersible, ALVIN, for fluid and rock sampling, the Autonomous Benthic Explorer (ABE) for mapping, and hydrocasts for characterizing the water column directly over the hydrothermal field. Other investigators have reported results from the first two of the three study components (Kelly et al., 2005; Brazelton et al., 2006, 2010, 2011, 2012; Ludwig et al., 2006, 2011; Proskurowski et al., 2006, 2008; Delacour et al., 2008a, 2008b; Lang et al., 2010, 2012, 2013). Here we report on the third component, the Lost City hydrothermal plume signature.

3.1. Hydrocast survey

The water column study consisted of 14 vertical hydrocasts in and around the seafloor hydrothermal system (Table 1, Fig. 2) designed to investigate the vertical position, and, to a lesser extent, the lateral scope of the plume as well as quantify the physical and chemical properties therein. All casts were conducted with a rosette equipped with a Seabird 911 plus conductivity-temperature-depth (CTD) package enhanced with a SBE 43 oxygen sensor, a Seapoint turbidity meter and an Eh sensor for measuring oxidation-reduction potential (e.g., German et al., 2008).

Nine of the 14 casts (Casts 3, 4, 6, 7, 8, 9, 12, 13, and 14) were conducted in close proximity to active venting. Six were conducted over the well-defined point sources in the southern portion of the field (Casts 3, 4, 6, 8, 9, and 12), and 3 other (Casts 7, 13, and 14) in the more nebulous and broadly distributed venting over a topographic saddle ~30 m to the north informally referred to as Chaff Beach (Kelley et al., 2001, 2005; Früh-Green et al., 2003; Ludwig et al., 2011). Two others casts (10 and 11) were performed at what were thought to be relict

hydrothermal sites. Two casts (1 and 5) were also performed about 1 km away to serve as background reference points, but samples were only taken from Cast #1, while sensor stability for several sensors was much better for Cast #5 than for Cast #1. Thus, cast #1 forms the basis for background gas data, while Cast #5 is the basis for background sensor data. Cast 2 was aborted due to communication problems, and no samples were taken.

All raw sensor data, except Eh, were processed by Seabird's Seasave software to produce the profiles shown in Fig. 3. Potential temperature (Fig. 3A) is calculated from temperature and depth readings and the seawater equation of state. Turbidity (Fig. 3B) is reported as Formazin Turbidity Units (FTU) and calculated as:

$$FTU = \frac{500 \times Scale\ Factor \times Voltage}{Cable\ Gain\ Setting} \quad (1)$$

where scale factor and cable gain setting are 1 and 100, respectively (Seapoint Sensors, Exeter, NH, USA). Conductivity voltages are converted to S/m using the sensor's known cell constant. Oxygen sensor phase shift (in seconds) is converted to concentration (mL/L) using the calibration established at Seabird prior to shipping. Concentration units are then converted to μmol/L assuming STP conditions in converting O_2 volume to moles.

Eh sensor data are transformed prior to output to the Seabird system to convert the data from their native range (300 to -150 mV) to an acceptable range for the Seabird system, (0 to 5 V). We recover the native data as:

$$Eh_{native} = -(Eh_{Seabird} \times 200 - 500) \quad (2)$$

where the negative sign accounts for installation of the electrodes in reverse order on the transformer for this cruise, a configuration that changes the sign of the voltage but does not otherwise affect the operation of the sensor. Eh data require processing in addition to the conversion shown in equation (2) as we discuss in the appendix.

3.2. Water Samples

The rosette was also equipped with 24 2L Niskin bottles used in collecting water samples for later chemical and microbiological analysis. Immediately upon recovery of the underwater sampling package, air-free water samples were flushed through 60-m-long sections of refrigeration grade Cu tubing with duplicate half-sections cold-weld sealed for later laboratory determinations of He concentration and isotope ratios (Young and Lupton, 1983). Isotope ratios and concentrations of helium were then determined at the NOAA/PMEL Helium Isotope Laboratory in Newport, OR USA using a dual collector, 21-cm-radius mass spectrometer. We report in Table 2 both absolute ^{3}He concentrations and background corrected values ($^3He^{\Delta}$), computed as the ^{3}He concentration of the sample minus the ^{3}He concentration of local

background seawater at the sample depth. The depth-dependent background ^3He concentration is taken from the ^3He profile from background Cast #1.

To determine CH_4 and H_2 concentrations, 100 ml of bubble-free fluid was drawn directly into 140 ml syringes followed by the addition of 40 ml headspace gas of ultra-pure helium The sample was vigorously shaken and allowed to warm to room temperature for about 30 min to reach equilibrium for H_2 and CH_4 between the water and gas phase. After equilibration, the headspace gas was injected into a SRI 8610C gas chromatograph. The separation of CH_4 and H_2 was accomplished with a 15 m long Molecular Sieve 5A column. H_2 concentrations were determined with a highly sensitive helium-pulsed discharge detector, and CH_4 concentrations were measured with a flame ionization detector (Kelley et al., 1998).

3.3. Data contouring

To assess variation in the extent and chemical makeup of the plume, we assemble the data in an East-West cross section (along the X-coordinate) for each of 4 properties: H_2, CH_4, $^3He^{\Delta}$, and dEh/dt_{TR} (Fig. 3E-H). To maximize data density for the cross section, we use all in field casts (3, 4, 6, 7, 8, 9, 12, 13, and 14) as well as the casts over the relict sites (10 and 11). The average Y position of the selected casts is between the main vent cluster (represented by Casts 3, 4, 6, 8, 9 and 12) and Chaff Beach (best captured by Casts 7, 13, and 14). Data from background casts provide a constraint on the ambient levels of the contoured properties. For the 3 profiles generated from discrete samples, we use background Cast #1 (the only casts where water samples were collected over the entire profile), located ~1100 m to the West of the vent field. For the dEh/dt_{TR} profile, we use discretized data from Cast #5 as described in the appendix. For both sample-based and sensor-based contours, in order to interpolate the data over the region of interest, it was necessary to replicate the western background cast to the east at an equivalent distance as the western cast. Interpolation is suppressed for points outside the dataset, such that all contours are bound by measurements. However, due to the difficulty in positioning the CTD package close to the bottom in this topographically challenging area, contours near the bottom have fewer data constraints than farther up in the water column. The final results of data contouring are shown in Fig. 4.

4. Results

Thirteen of the fourteen hydrocasts conducted yielded good results for most sensors; however, sensor data from the second background Cast (#5) are more trustworthy than the first background Cast (#1) for which several sensors had not yet been sufficiently conditioned to give stable readings. Samples were also not collected from hydrocast #5, which was a repeat of background Cast #1, and samples from Casts 12, 13, or 14 were not analyzed for ^3He.

4.1. Temperature, turbidity, conductivity, and oxygen

Four of the five sensor profiles (potential temperature, turbidity, conductivity, and oxygen) show almost no evidence in the water column of the underlying hydrothermal venting with the exception of a single cast (#14) which captured anomalies in potential temperature (~0.2 °C) and conductivity (~0.05 S/m) at ~800 m below sea level (mbsl) (Fig. 3A-D). Casts directly over the most pronounced venting (Casts 3 and 4) are indistinguishable in both potential temperature (Fig. 3A) and conductivity (Fig. 3C) compared to background Cast 5. The turbidity signal may show a slight blip (~0.005 FTU) at ~800 m (Fig. 3B), but the higher signal to noise ratio of this profile precludes a firm positive ID. We generally see more spread in the oxygen profiles than in potential temperature, conductivity and turbidity, but much of this occurs between 200 and 500 mbsl, at least 300 m above the active venting (not shown). We also observe some slight variability between oxygen profiles at ~600-700 mbsl (between 150 and 165 μmol/kg), but there is no correlation between variability in the profiles and proximity to venting.

4.2. dEh/dt_{TR}, H_2, CH_4, and $^3He^{\Delta}$

In contrast to potential temperature, conductivity, turbidity and oxygen, the dEh/dt_{TR} sensor profiles (Fig. 3E) exhibit a strong uptick in casts conducted in and around the vent field (Casts 3, 4, 6, 7, 8, 9, 12, 13, and 14) compared to casts conducted near and far afield (Casts 11 and 5 respectively), which register no such increase. A slight anomaly is also visible in Cast 10, and though mild compared to other near-field casts, it manifests in all 4 plume-sensitive properties (H_2, CH_4, dEh/dt_{TR} and very slightly in $^3He^{\Delta}$), and at 300 m away from the main vent cluster, represents the most far flung indicator of venting. Cast #9 near Marker H shows the largest negative peak in dEh/dt_{TR} (-1879 mV/s) followed closely by two such peaks in Cast #6 (reaching up to -1772 mV/s). The dEh/dt spike in Cast #9 is accompanied by spikes in CH_4 (~180 nM, Fig. 3F) and $^3He^{\Delta}$ (0.7 fmol/kg, Fig. 3G) that are also the largest observed for these two data types; while the Cast 6 dEh/dt_{TR} signal is similarly replicated in CH_4 and $^3He^{\Delta}$, the magnitude of the signal is lower. We observed elevated H_2 in Casts 6 and 9, (Fig. 3H), but the largest spikes in H_2 (reaching up to 350 nM) occur in Casts 7 and 14, which are positioned closer to Marker 7 and Chaff Beach than the southern cluster of vents down slope (Fig. 2). We see moderate peaks in CH_4 (~50 nM), $^3He^{\Delta}$ (0.38 fmol/kg), and dEh/dt_{TR} (-237 mV/s) in Cast 7, and in CH_4 (~50 nM) and dEh/dt_{TR} (-622 mV/s) in Cast 13. Casts 4 and 8 also captured elevated but overall lower concentrations of H_2, CH_4, and $^3He^{\Delta}$. Cast #3, one of the 2 closest to intense venting at the largest and most remarkable chimney in the field, Poseidon (Kelley et al., 2005), showed relatively minor elevations in all dissolved volatiles. The full results of water sample analysis are shown in Table 2 alongside the corresponding dEh/dt_{TR} value at the depth the bottle was fired.

4.3. Plume cross sections

There are several local H_2 maxima in the plume cross section (Fig. 4D). The most significant (~250 nM) is located at ~800 m, situated between Markers 8 and 2, and constrained

by samples from Cast 8 and the lower portion of Cast 7. The second largest anomaly manifests as a distinct island hovering at ~750 m, just above the lower plume and shifted slightly to the west and defined by a combination of samples taken over Chaff Beach (Casts 13 and 7) and the main vent cluster (Casts 4 and 6). A third anomaly, situated between these two depths (~775 m), lies off to the east over Marker H, and is captured by samples from both northern (cast 14 over Chaff Beach) and southern (Cast 9 over Marker H) profiles. H_2, with its 3 well-defined maxima, is unique in its distribution among the 4 plume properties shown in Fig. 4.

The remaining 3 properties exhibit the largest anomaly at ~850 (right at the seafloor) centered over Marker H and captured in all 3 metrics by a significant peak in Cast 9. The CH_4 anomaly (~150 nM) extends up and to the west, with two other minor anomalies in positions similar to the H_2 maxima but relatively less pronounced (Fig. 4B). dEh/dt_{TR} is similar in its distribution to CH_4, with the seafloor-adjacent anomaly reaching up approximately -1600 mV/s (Fig. 4A). dEh/dt_{TR} does not exhibit the eastern anomaly over Marker H, and the shallow island anomaly (~725 m for dEh/dt) makes a stronger showing in peak magnitude than the analogous feature for CH_4. For both CH_4 and dEh/dt_{TR}, the island anomaly in the cross sections derives from the same combination of casts and samples as those that define the H_2 island (Casts, 4, 6, 13 and a portion of 7). $^3He^{\Delta}$ shows only the seafloor-adjacent anomaly (~0.45 fmol/kg), while both the shallow island feature and the eastern anomaly are missing (Fig. 4C). However, as no data are available for Casts 12, 13 and 14 for this parameter, the missing features may not have been sampled.

For all 4 of the properties shown in cross section, the contours on the western side are influenced by a single sample from Cast 10, which reflects the only measured anomaly not in the immediate vicinity of the main field.

5. Discussion

The extent of deep-sea venting from mid-ocean ridge (MOR) hydrothermal fields situated on the axis of the ridge has been increasingly well documented since the discovery of seafloor venting (Baker and German, 2004). In contrast, serpentinzation-related hydrothermal activity in off-axis settings, such as at Lost City, is a relatively recent discovery (Kelley et al., 2001). However, this style of venting may be an important, if elusive, partner to on-axis venting in the delivery of reduced carbon from the earth's interior to the overlying ocean. We present below a more detailed picture of the physical and chemical makeup of the Lost City vent plume and how it compares to other known hydrothermal systems.

5.1. Stealth venting

Hydrothermal output from the Lost City vent field, located 15 km from the Mid-Atlantic mid-ocean ridge (MOR), presents a unique signature compared to vent fields located directly on a ridge axis. Whereas the latter frequently manifest strong signals in potential temperature,

dEh/dt_{TR} and turbidity owing to the extremely hot, reducing, and particulate-laden fluids venting from the seafloor (Baker and Massoth, 1987; Feely et al., 1990), the Lost City plume eluded all real-time methods of detection except Eh. The venting fluid has a relatively low temperature (with a maximum of ~90 °C) compared to black smoker fluids (which can reach in excess of 400 °C), and the high dissolved metal content that leads to the metal sulfide particles that form the 'smoke' in black smokers is simply not present in the low temperature serpentinization circulation and venting undergirding the Lost City plume. Although the Lost City plume is unremarkable in many of the metrics used to identify black-smoker style venting, the concentration of dissolved volatiles rivals or, in some cases, far exceeds gas concentrations in typical on-axis plumes (Lilley et al. 1995; McDuff, 1995). With H_2 and CH_4 concentrations reaching up to 350 nM and 180 nM, respectively, (Fig. 3E, F), this style of venting provides an avenue for export of appreciable quantities of reduced volatiles to the deep sea in a manner that is nearly invisible to detection.

Locating a new field similar to Lost City may therefore require adapting current approaches to focus on the water signatures that persist away from the site of venting. Any such scouting will undoubtedly start with consideration of geologic context, a powerful tool for the educated prediction of sites of significant chemical exchange between the earth and deep ocean. Indeed, the research leading to the discovery of Lost City itself was based on interest in a seamount on the inside corner of a MOR transform fault (Blackman et al., 2002). Real time sensing of redox potential remains a viable tool for 'invisible' plume detection because it works even for plumes devoid of particle anomalies (Henry et al., 2002), and this method suggests widespread occurrence of Eh anomalies along unexplored portions of the mid-ocean ridge (Baker et al., 2013). However, the relatively rapid disappearance of the redox signal within ~1 km of a source (Stranne et al., 2010) limits the spatial extent that can be explored with this technique. Though once a region has been identified, new developments in automated plume hunting can extend the reach of Eh sensing capability by using data from on-board sensors to automatically calculate course corrections in exploration routes of unmanned vehicles (Yoerger et al., 2007).

Given our detection of anomalies ~400 m away from the main field (e.g., Cast 10) and the spatial scales on which Eh plume detection operates, a combination of Eh sensing and autonomous vehicles could play an important role in future discoveries. Nevertheless, other real time sensing capabilities will be essential to ocean exploration. From the current study, we see that CH_4 and dEh/dt_{TR} exhibit some correlation (a relationship even more pronounced after Eh data processing, as described in the appendix). Furthermore CH_4 is known to be longer lived in hydrothermal plumes than other reducing species (Lilley et al., 1995), so real time sensing of CH_4 could be a valuable exploration tool. In fact, in-situ measurement of CH_4 is already possible with existing technology (Newman et al., 2008), though long response times could reduce the effectiveness of this tool (Lamontagne et al., 2001).

5.2. Identification of Plume Sources and Importance of Beach-type venting

Connecting the water column signals to their origins in the vent field highlights the transformations that occur to fluids after exiting the seafloor and brings to light a distinct form of venting. The sources of water column signals can be constrained through vent depths, physical locations, and H_2/CH_4 ratios. Depth can be used to eliminate some vents as a potential source of water column anomalies because initially buoyant plume fluid can only be supplied by vents at greater depth. Physical locations are less useful since strong water currents that shift in direction can be present in the field. The H_2/CH_4 ratio provides an additional source constraint. Previous studies demonstrate that H_2 is oxidized in the water column approximately 20 times faster than CH_4 (Kadko et al., 1990; Lilley et al., 1995), resulting in lower H_2/CH_4 ratios with increasing distance from a vent source (Lilley et al., 1995; Kelley et al., 1998; Marbler et al., 2010). Therefore, water column H_2/CH_4 signatures can only be sourced by vents with higher H_2/CH_4 ratios. Table 3 provides a summary that compares depths of identified vent chimneys, the depth of the strongest water column plume signals, and H_2/CH_4 ratios.

In most cases the water column signals have multiple potential sources; however, there are two instances where it is possible to attribute the signatures to individual vents. Cast 9 captured elevated CH_4, dEh/dt_{TR} and $^3He^{\Delta}$ anomalies along with a decreased H_2/CH_4 ratio. These features most likely originated from the focused vent, Marker H, a down-slope point source on the eastern side of the field. It is the only know venting site that is deep enough to produce a plume at 830 m depth, and it has a H_2/CH_4 ratio (~0.9) comparable to the ratio measured in the plume. Similarly, we postulate that the signatures from Cast 14 originated from Marker C because it is the only vent whose depth and H_2/CH_4 ratio are greater than the plume feature. While the shallower anomaly in Cast 7 (X coordinate = 6080, depth = 741 m) cannot be traced to a single source, the depth and H_2/CH_4 ratio of this signal can be used to narrow the source down to 2 identified vents: Markers 6 or C.

The lower anomaly of Cast 7 (depth = 794 m) is more provocative. The H_2/CH_4 ratio is higher than all the known focused vent sources of greater depth (Table 3) and so cannot be easily attributed to a point source. The most likely source for this elevated H_2/CH_4 ratio is Chaff Beach, a gently sloping area at around 800 m depth and greater, which is covered with carbonate ooze that has been variably cemented by hydrothermally derived carbonate crust (Kelley et al., 2001; 2005; Blackman et al., 2002; Früh-Green et al., 2003; Karson et al., 2006; Luwdig et al., 2011). Direct visual observation of a widespread surface of shimmering diffuse flow is consistent with this interpretation (ALVIN dive reports, 3865). The Alvin high temperature probe recorded in the sediments a temperature of ~0.25°C above background seawater.

The source of the plume signal in Cast #10, which was taken at a location ~400 m west of the main field, also has relatively high H_2/CH_4 ratios and, given the distance from the main field, is unlikely to be due to identified vents. The source of this signal may indicate an additional

region of active venting located on a newly mapped but currently assumed extinct hydrothermal mound (Denny et al., in preparation).

The relatively high H_2/CH_4 ratios in these two locations may reflect differences in the way hydrothermal fluid escapes the subsurface as well as in the consumption and production of dissolved volatiles prior to their release. In the focused flow of the main vent chimneys, fluids with higher H_2/CH_4 ratios are associated with higher temperature fluids, while those with lower H_2/CH_4 ratios have been influenced by microbial sulfate reduction (Proskurowski et al., 2006; Lang et al., 2012). These higher temperatures (60-91°C) may preclude the growth of sulfate reducing bacteria; the cultivated species that are most closely related to those found in the carbonate chimneys have optimum growth temperatures <55˚C (Lang et al., 2012).

Microbial sulfate reduction is not temperature limited in the warm fluids at Chaff Beach, but the H_2/CH_4 ratios remain curiously high. A speculative but feasible explanation for this observation is that these diffuse fluids are more extensively reacted with the rock than those that supply the main field. In this scenario, serpentinization continues to produce H_2 even after the 1-4 mM sulfate present in the fluid supplying the field as a whole (and evident in fluids with higher temperatures) has been exhausted. The implication is that Chaff Beach fluids have longer residence times than channelized chimney fluids, and that the flow paths underlying the Beach environment are inaccessible to infiltration by SO_4-rich seawater. This scenario would be akin to continental serpentinization environments where the lack of sulfate in meteoric waters can result in gas bubbles that are almost pure hydrogen (Neal and Stanger, 1983).

5.3. Oxidation

To distinguish between processes that added or removed H_2 and CH_4 from the samples, the gas concentrations were first normalized to the content of $^3He^{\Delta}$ in the same fluids. $^3He^{\Delta}$ is a non-reactive tracer of mantle-derived volatiles and is used here to account for the effects of mixing and dilution of hydrothermal fluids with deep seawater. The $CH_4/^3He^{\Delta}$ content of endmember source fluids ranges from 351-570 x 10^6, while that of $H_2/^3He^{\Delta}$ ranges from 529-4485 x 10^6 (Proskurowski et al., 2008). Clear evidence that oxidation of these volatile species continues in the plume comes from the lower ratios that are found in the plume fluids, from 0.04 – 243 x 10^6 for $CH_4/^3He^{\Delta}$ and 3.6 – 1600 x 10^6 for $H_2/^3He^{\Delta}$ (Fig. 5).

There may be some natural variability in the initial $H_2/^3He^{\Delta}$ content of the fluids as the reactions leading to H_2 production in the subsurface are not directly linked to magma degassing. The large range of values in endmember fluids has also been attributed to oxidation of the H_2 during sulfate reduction (Proskurowski et al., 2006; Lang et al., 2012). The more narrow range of $CH_4/^3He^{\Delta}$ values may reflect the closer coupling of CH_4 production and magmatic degassing, if the initial carbon source of the CH_4 is magmatic CO_2. This relationship has been previously inferred based in part on the lack of ^{14}C in the methane which precludes deep-sea inorganic

carbon as the starting carbon material (Proskurowski et al., 2008). In addition, CH_4 appears to have been influenced to a lesser extent by biological production or consumption processes in endmember fluids. This does not mean that methane is not, to some extent, produced or consumed by microbial processes but rather that any biological signal is relatively small compared to the abiogenic signal.

The high concentrations of H_2 and CH_4 are a characteristic feature of ultramafic systems. Compared to other ultramafic systems on the Mid-Atlantic Ridge, the ratios of $CH_4/^3He^{\Delta}$ and $H_2/^3He^{\Delta}$ are somewhat higher owing in part to the lower magmatic contribution at Lost City compared to the axial systems (Fig. 5). For example, Rainbow, Logatchev, and Drachenschlund have $CH_4/^3He^{\Delta}$ ratios of ~100 – 400 x 10^6 (compared to 351-570 x 10^6 at Lost City) and $H_2/^3He^{\Delta}$ ratios of ~475-3430 x 10^6 (compared to 529-4485 x 10^6 at Lost City; Charlou et al., 2000, 2002, 2010; Lein et al., 2000; Jean-Baptiste et al., 2004; Proskurowski et al., 2006, 2008; Keir et al., 2008, 2009; Melchert et al., 2008).

The export of these reduced gases to the deep sea is of interest from a global flux perspective and as a potential energy source for microbial communities. For that reason, it is also of interest *where* H_2 and CH_4 are consumed or lost (e.g., before or after venting), as it may account for variability in flux estimates or point to specific microbial metabolisms at work, such as the difference between hydrogen being consumed during sulfate reduction or during hydrogen oxidation with O_2. We therefore compared the extent of oxidation that occurred in fluids prior to exiting the vent orifice, where it presumably occurred anaerobically (e.g., sulfate reduction), to the fluids in the water column, where aerobic reactions dominate (e.g., the knallgas reaction). For this comparison we used the highest values of $CH_4/^3He^{\Delta}$ and $H_2/^3He^{\Delta}$ and assumed that any lower values were due to oxidation (Fig. 6). This approach ignores natural variability in the ratios that may be due to other processes, and maximizes the calculated amount of oxidation. Despite this, a maximum of 40% of the CH_4 oxidation occurs in the anaerobic subsurface while the remaining 60% occurs in the plumes.

In contrast to the methane, which is to some extent stable enough to be exported into the water column and be detected in the plume, the vast majority of the hydrogen is oxidized by the time it is sampled in the plume. As discussed earlier, the loss of H_2 begins within the anaerobic subsurface as the result of sulfate reduction, and some of the vent fluids have already lost almost 90% of their initial hydrogen. Interestingly, two samples from Cast #7 had higher $H_2/^3He^{\Delta}$ ratios than some endmember vent fluids (manifested as a lower percentage on the y-axis lost in Fig. 6). These samples were collected from north of the main vent cluster, above the flat Chaff Beach. This cast also had a big increase in dEh/dt_{TR}. The largest export of H_2 into the water column at the Lost City field may come from this visually unimpressive area.

The oxidation of H_2 and CH_4 is decoupled. As discussed in section 5.2, the differences in concentrations for the two species differ, at least in part, to their point of issuance from the seafloor. However, even beyond differences between central and peripheral source, H_2 and CH_4 concentrations exhibit distinctive patterns. Whereas CH_4 oxidation is split almost evenly between subsurface and plume, hydrogen oxidation is largely confined to the subsurface. The implication is that in the case of H_2, even though concentrations are relatively high for a plume environment, most H_2 does not make it into the water column. Conversely, a substantial amount of CH_4 routinely finds its way from the subsurface to the water column where it can nourish plume communities. Chaff Beach presents an exception to this narrative, holding out the possibility that this style of unfocused but broadly distributed venting may yet be a significant contributor of hydrogen to the deep sea.

6. Conclusion

Hydrothermal venting from the Lost City on the Mid-Atlantic Ridge delivers high concentrations of H_2 and CH_4 to the deep sea in hydrothermal fluids that are relatively low in temperature and free of particulates compared to MOR hydrothermal fluids with similar concentrations of dissolved gas. This presents an obstacle to the discovery of this style of venting because temperature and turbidity are two metrics typically used in the exploration for seafloor hydrothermal systems. Lost City hydrothermal circulation does generate a strong dEh/dt_{TR} signal, aiding exploration efforts overcome what might otherwise be the insurmountable hurdle of finding a 6 km^2 patch of venting, the metaphorical needle in the 360 million km^2 haystack that is the ocean floor. Even so, the Lost City's geographic location, far away from the MOR axis where exploration efforts are focused, makes the discovery of this style of venting uncomfortably dependent on serendipity.

The stealth character of Lost City venting is notable because it represents the delivery of biogeochemically relevant species (H_2 and CH_4) to the deep sea in a way that may not be adequately captured by current estimates of biogeochemical fluxes that are based on readily identifiable sources and sinks (e.g., German et al., 2010). Indeed, the highest observed H_2 concentration is observed over Chaff Beach, an area with no obvious vent features. Furthermore, plume samples taken over Chaff Beach also exhibit the lowest degree of oxidative loss of H_2 (based on normalization to $^3He^{\Delta}$), suggesting that the fluid source producing this plume may be an even more important source of H_2 than the more identifiable cluster of chimneys in the South. Thus, even bathymetry - often used in guiding exploration efforts (Lowell et al., 1995; Baker and German, 2004) - would fail in this case - along with temperature and turbidity - to point to the existence of a potentially significant seafloor source of dissolved H_2.

Unlike H_2, CH_4 behaves a bit more traditionally, with the highest concentrations centered over the area of identifiable point sources. Another notable difference between the H_2 and CH_4 species is that, while H_2 oxidation occurs largely in the subsurface, greater than half of the

oxidative loss of CH_4 transpires in the water column. This consistent export of CH_4 in Lost City plume water – combined with the invisibility of the plume to most traditional metrics and location of the site in a geologic setting of the kind that is largely unexplored – supports the possibility that consequential sources of CH_4 in the deep sea may remain undiscovered.

Acknowledgements
We thank the captains and crews of the R/V *Atlantis*, R/V *Ronald H. Brown,* DSV *Alvin,* ROV *Hercules* and ABE for their invaluable assistance and Deborah Kelley for her leadership as chief scientist. This work was supported by NSF grant OCE0137206 and partially funded by the PMEL Earth-Ocean Interactions Program and the Joint Institute for the Study of the Atmosphere and Ocean (JISAO) under NOAA Cooperative Agreement No. NA10OAR4320148.
This is JISAO Contribution Number 2406, and PMEL Contribution Number 4272.

References

Abrajano, T.A., Sturchio, N.C., Bohlke, J.K., Lyon, G.L., Poreda, R.J., Stevens, C.M., 1988. Methane-hydrogen gas seeps, Zambales Ophiolite, Philippines - deep or shallow origin? Chem. Geol. 71, 211-222.

Abrajano, T.A., Sturchio, N.C., Kennedy, B.M., Lyon, G.L., Muehlenbachs, K., Bohlke, J.K., 1990. Geochemistry of reduced gas related to serpentinization of the Zambales Ophiolite, Philippines. Appl. Geochem. 5, 625-630.

Baker, E.T., German, C.R., 2004. On the Global Distribution of Hydrothermal Vent Fields, in: German, C.R., Lin, J., Parson, L.M. (Eds.), Mid-Ocean Ridges. American Geophysical Union, Washington, pp. 245-266.

Baker, E.T., Massoth, G.J., 1987. Characteristics of hydrothermal plumes from two vent fields on the Juan de Fuca Ridge, northeast Pacific Ocean. Earth Planet. Sci. Lett. 85, 59-73.

Baker, E.T., Resing, J.A., Martinez, F., Haymon, R.M., Nakamura, K., Walker, S.L., Ferrini, V., 2013. How Leaky Are Seafloor Spreading Center Axes? AGU Fall Meeting Abstracts 41, 1831.

Barnes, I., Oneil, J.R., Trescases, J.J., 1978. Present Day serpentinization in New-Caledonia, Oman and Yugoslavia. Geochim. Cosmochim. Acta 42, 144-145.

Blackman, D.K., Karson, J.A., Kelley, D.S., Cann, J.R., Fruh-Green, G.L., Gee, J.S., Hurst, S.D., John, B.E., Morgan, J., Nooner, S.L., Ross, D.K., Schroeder, T.J., Williams, E.A., 2002. Geology of the Atlantis Massif (Mid-Atlantic Ridge, 30 degrees N): Implications for the evolution of an ultramafic oceanic core complex. Marine Geophysical Research 23, 443-469.

Blank, J.G., Green, S., Blake, D., Valley, J.W., Kita, N.T., Treiman, A., Dobson, P.F., 2009. An alkaline spring system within the Del Puerto Ophiolite (California, USA): A Mars analog site. Planetary and Space Science 57, 533-540.

Boschi, C., Dini, A., Früh-Green, G.L., Kelley, D.S., 2008. Isotopic and element exchange during serpentinization and metasomatism at the Atlantis Massif (MAR 30 N): insights from B and Sr isotope data. Geochim. Cosmochim. Acta 72, 1801-1823.

Brazelton, W.J., Ludwig, K.A., Sogin, M.L., Andreishcheva, E.N., Kelley, D.S., Shen, C.-C., Edwards, R.L., Baross, J.A., 2010. Archaea and bacteria with surprising microdiversity show shifts in dominance over 1,000-year time scales in hydrothermal chimneys. Proceedings of the National Academy of Sciences 107, 1612-1617.

Brazelton, W.J., Mehta, M.P., Kelley, D.S., Baross, J.A., 2011. Physiological differentiation within a single-species biofilm fueled by serpentinization. MBio 2, e00127-00111.

Brazelton, W.J., Nelson, B., Schrenk, M.O., 2012. Metagenomic Evidence for H(2) Oxidation and H(2) Production by Serpentinite-Hosted Subsurface Microbial Communities. Frontiers in Microbiology 2, Article 268.

Brazelton, W.J., Schrenk, M.O., Kelley, D.S., Baross, J.A., 2006. Methane- and sulfur-metabolizing microbial communities dominate the Lost City hydrothermal field ecosystem. Appl. Environ. Microbiol. 72, 6257-6270.

Cannat, M., Fontaine, F., Escartin, J., 2010. Serpentinization and hydrothermal venting at slow-spreading ridges. Geochim. Cosmochim. Acta 74, A138-A138.

Charlou, J.L., Donval, J.P., Douville, E., Jean-Baptiste, P., Radford-Knoery, J., Fouquet, Y., Dapoigny, A., Stievenard, M., 2000. Compared geochemical signatures and the evolution of Menez Gwen (37 degrees 50 ' N) and Lucky Strike (37 degrees 17 ' N) hydrothermal fluids, south of the Azores Triple Junction on the Mid-Atlantic Ridge. Chem. Geol. 171, 49-75.

Charlou, J.L., Donval, J.P., Fouquet, Y., Jean-Baptiste, P., Holm, N., 2002. Geochemistry of high H2 and CH4 vent fluids issuing from ultramafic rocks at the Rainbow hydrothermal field (36 degrees 14 ' N, MAR). Chem. Geol. 191, 345-359.

Charlou, J.L., Donval, J.P., Konn, C., OndréAs, H., Fouquet, Y., Jean-Baptiste, P., Fourré, E., 2010. High production and fluxes of H2 and CH4 and evidence of abiotic hydrocarbon synthesis by serpentinization in ultramafic-hosted hydrothermal systems on the Mid-Atlantic Ridge, Diversity Of Hydrothermal Systems On Slow Spreading Ocean Ridges. American Geophysical Union, pp. 265-296.

Chartrand, R., 2011. Numerical differentiation of noisy, nonsmooth data. ISRN Applied Mathematics 2011, Article ID 164564, 11 pages. doi:10.5402/2011/164564.

Cipolli, F., Gambardella, B., Marini, L., Ottonello, G., Zuccolini, M.V., 2004. Geochemistry of high-pH waters from serpentinites of the Gruppo di Voltri (Genova, Italy) and reaction path modeling of CO2 sequestration in serpentinite aquifers. Appl. Geochem. 19, 787-802.

Delacour, A., Fruh-Green, G.L., Bernasconi, S.M., Kelley, D.S., 2008a. Sulfur in peridotites and gabbros at Lost City (30 degrees N, MAR): Implications for hydrothermal alteration and microbial activity during serpentinization. Geochim. Cosmochim. Acta 72, 5090-5110.

Delacour, A., Fruh-Green, G.L., Bernasconi, S.M., Schaeffer, P., Kelley, D.S., 2008b. Carbon geochemistry of serpentinites in the Lost City hydrothermal system (30 degrees N, MAR). Geochim. Cosmochim. Acta 72, 3681-3702.

Denny A., Kelly. D.S. In Preparation. Geologic Evolution of the Lost City Hydrothermal Field.

Etiope, G., Schoell, M., Hosgormez, H., 2011. Abiotic methane flux from the Chimaera seep and Tekirova ophiolites (Turkey): Understanding gas exhalation from low temperature serpentinization and implications for Mars. Earth Planet. Sci. Lett. 310, 96-104.

Feely, R.A., Geiselman, T.L., Baker, E.T., Massoth, G.J., Hammond, S.R., 1990. Distribution and composition of hydrothermal plume particles from the ASHES vent field at Axial Volcano, Juan de Fuca Ridge. J. Geophys. Res.-Solid 95, 12855-12873.

Fritz, P., Clark, I.D., Fontes, J.C., Whiticar, M.J., Faber, E., 1992. Deuterium and 13C evidence for low temperature production of hydrogen and methane in a highly alkaline groundwater environment in Oman, in: Kharaka, Y.K., Maest, A.S. (Eds.), Proceedings of the 7th International Symposium on Water–rock Interaction, Edmonton, AB, pp. 793-796.

Früh-Green, G.L., Kelley, D.S., Bernasconi, S.M., Karson, J.A., Ludwig, K.A., Butterfield, D.A., Boschi, C., Proskurowski, G., 2003. 30,000 years of hydrothermal activity at the Lost City vent field. Science 301, 495-498.

Garcia, D., 2010. Robust smoothing of gridded data in one and higher dimensions with missing values. Computational statistics & data analysis 54, 1167-1178.

German, C., Thurnherr, A., Knoery, J., Charlou, J.-L., Jean-Baptiste, P., Edmonds, H., 2010. Heat, volume and chemical fluxes from submarine venting: A synthesis of results from the Rainbow hydrothermal field, 36 N MAR. Deep-Sea Res. Pt. I 57, 518-527.

German, C.R., Von Damm, K.L., 2003. Hydrothermal Processes, in: Elderfield, H. (Ed.), Treatise on Geochemistry. Pergamon, Oxford, pp. 181-222.

German, C.R., Yoerger, D.R., Jakuba, M., Shank, T.M., Langmuir, C.H., Nakamura, K.-i., 2008. Hydrothermal exploration with the Autonomous Benthic Explorer. Deep-Sea Res. Pt. I 55, 203-219.

Hansen, P. C., 2010. Discrete inverse problems: Insight and algorithms. Philadelphia, Pa: Society for Industrial and Applied Mathematics.

Hansen, P.C., Nagy, J.G., O'leary, D.P., 2006. Deblurring images: Matrices, spectra, and filtering. Philadelphia, PA: Society for Industrial and Applied Mathematics.

Henry, P., Lallemant, S., Nakamura, K.-i., Tsunogai, U., Mazzotti, S., Kobayashi, K., 2002. Surface expression of fluid venting at the toe of the Nankai wedge and implications for flow paths. Marine Geology 187, 119-143.

Hosgormez, H., Etiope, G., Yalcin, M.N., 2008. New evidence for a mixed inorganic and organic origin of the Olympic Chimaera fire (Turkey): a large onshore seepage of abiogenic gas. Geofluids 8, 263-273.

Jean-Baptiste, P., Fourre, E., Charlou, J.L., German, C.R., Radford-Knoery, J., 2004. Helium isotopes at the Rainbow hydrothermal site (Mid-Atlantic Ridge, 36 degrees 14 ' N). Earth Planet. Sci. Lett. 221, 325-335.

Jiang, Yuan. Solving the Inverse Problem of Electrocardiography in a Realistic Environment. Karlsruhe Transactions On Biomedical Engineering. Vol. 9. Karlsruhe, Germany: KIT Scientific Publishing, 2010.

Johnston, P.R., Gulrajani, R.M., 2000. Selecting the corner in the L-curve approach to Tikhonov regularization. Biomedical Engineering, IEEE Transactions on 47, 1293-1296.

Kadko, D.C., Rosenberg, N.D., Lupton, J.E., Collier, R.W., Lilley, M.D., 1990. Chemical-reaction rates and entrainment within the Endeavor Ridge hydrothermal plume. Earth Planet. Sci. Lett. 99, 315-335.

Karson, J.A., Fruh-Green, G.L., Kelley, D.S., Williams, E.A., Yoerger, D.R., Jakuba, M., 2006. Detachment shear zone of the Atlantis Massif core complex, Mid-Atlantic Ridge, 30 degrees N. Geochem. Geophys. Geosyst. 7, 6. Q06016, doi:10.1029/2005GC001109.

Keir, R.S., 2010. A note on the fluxes of abiogenic methane and hydrogen from mid-ocean ridges. Geophys. Res. Lett. 37, 5.

Keir, R.S., Schmale, O., Seifert, R., Sultenfuss, J., 2009. Isotope fractionation and mixing in methane plumes from the Logatchev hydrothermal field. Geochem. Geophys. Geosyst. 10, 5. Q05005, doi:10.1029/2009GC002403.

Keir, R.S., Schmale, O., Walter, M., Silltenfuss, J., Seifert, R., Rhein, M., 2008. Flux and dispersion of gases from the "Drachenschlund" hydrothermal vent at 8 degrees 18'S, 13 degrees 30'W on the Mid-Atlantic Ridge. Earth Planet. Sci. Lett. 270, 338-348.

Kelley, D.S., Karson, J.A., Blackman, D.K., Fruh-Green, G.L., Butterfield, D.A., Lilley, M.D., Olson, E.J., Schrenk, M.O., Roe, K.K., Lebon, G.T., Rivizzigno, P., Party, A.T.S., 2001. An off-axis hydrothermal vent field near the Mid-Atlantic Ridge at 30 degrees N. Nature 412, 145-149.

Kelley, D.S., Karson, J.A., Fruh-Green, G.L., Yoerger, D.R., Shank, T.M., Butterfield, D.A., Hayes, J.M., Schrenk, M.O., Olson, E.J., Proskurowski, G., Jakuba, M., Bradley, A., Larson, B., Ludwig, K., Glickson, D., Buckman, K., Bradley, A.S., Brazelton, W.J., Roe, K., Elend, M.J., Delacour, A., Bernasconi, S.M., Lilley, M.D., Baross, J.A., Summons, R.T., Sylva, S.P., 2005. A serpentinite-hosted ecosystem: The lost city hydrothermal field. Science 307, 1428-1434.

Kelley, D.S., Lilley, M.D., Lupton, J.E., Olson, E.J., 1998. Enriched H-2, CH4, and He-3 concentrations in hydrothermal plumes associated with the 1996 Gorda Ridge eruptive event. Deep-Sea Res. Pt. II 45, 2665-2682.

Lamontagne, R., Rose-Pehrsson, S., Grabowski, K., Knies, D., 2001. Response of METS Sensor to Methane Concentrations found on the Texas-Louisiana Shelf in the Gulf of Mexico. Washington DC: Naval Research Laboratory, Report number NRL/MR/6110-01-8584 ,13 pp.

Lang, S.Q., Butterfield, D.A., Schulte, M., Kelley, D.S., Lilley, M.D., 2010. Elevated concentrations of formate, acetate and dissolved organic carbon found at the Lost City hydrothermal field. Geochim. Cosmochim. Acta 74, 941-952.

Lang, S.Q., Fruh-Green, G.L., Bernasconi, S.M., Butterfield, D.A., 2013. Sources of organic nitrogen at the serpentinite-hosted Lost City hydrothermal field. Geobiology 11, 154-169.

Lang, S.Q., Fruh-Green, G.L., Bernasconi, S.M., Lilley, M.D., Proskurowski, G., Mehay, S., Butterfield, D.A., 2012. Microbial utilization of abiogenic carbon and hydrogen in a serpentinite-hosted system. Geochim. Cosmochim. Acta 92, 82-99.

Lartaud, F., Little, C.T.S., de Rafelis, M., Bayon, G., Dyment, J., Ildefonse, B., Gressier, V., Fouquet, Y., Gaill, F., Le Bris, N., 2011. Fossil evidence for serpentinization fluids fueling chemosynthetic assemblages. Proc. Natl. Acad. Sci. U. S. A. 108, 7698-7703.

Lein, A.Y., Grichuk, D.V., Gurvich, E.G., Bogdanov, Y.A., 2000. A new type of hydrogen- and methane-rich hydrothermal solutions in the rift zone of the Mid-Atlantic Ridge. Dokl. Earth Sci. 375, 1391-1394.

Lilley, M.D., Feely, R.A., Trefry, J.H., 1995. Chemical and Biochemical Transformations in Hydrothermal Plumes, in: Humphris, S.E. (Ed.), Seafloor Hydrothermal Systems: Physical, Chemical, Biological, and Geological Interactions. American Geophysical Union, Washington, D. C., pp. 369-391.

Lowell, R.P., Rona, P.A., Von Herzen, R.P., 1995. Seafloor hydrothermal systems. J. Geophys. Res.-Sol. Ea. 100, 327-352.

Ludwig, K.A., Kelley, D.S., Butterfield, D.A., Nelson, B.K., Fruh-Green, G., 2006. Formation and evolution of carbonate chimneys at the Lost City Hydrothermal Field. Geochim. Cosmochim. Acta 70, 3625-3645.

Ludwig, K.A., Shen, C.C., Kelley, D.S., Cheng, H., Edwards, R.L., 2011. U-Th systematics and Th-230 ages of carbonate chimneys at the Lost City Hydrothermal Field. Geochim. Cosmochim. Acta 75, 1869-1888.

Marbler, H., Koschinsky, A., Pape, T., Seifert, R., Weber, S., Baker, E.T., de Carvalho, L.M., Schmidt, K., 2010. Geochemical and physical structure of the hydrothermal plume at the ultramafic-hosted Logatchev hydrothermal field at 14 degrees 45 ' N on the Mid-Atlantic Ridge. Marine Geology 271, 187-197.

Marques, J.M., Carreira, P.M., Carvalho, M.R., Matias, M.J., Goff, F.E., Basto, M.J., Graca, R.C., Aires-Barros, L., Rocha, L., 2008. Origins of high pH mineral waters from ultramafic rocks, Central Portugal. Appl. Geochem. 23, 3278-3289.

McDuff, R.E., 1995. Physical Dynamics of Deep-Sea Hydrothermal Plumes, in: Humphris, S.E. (Ed.), Seafloor Hydrothermal Systems: Physical, Chemical, Biological, and Geological Interactions. American Geophysical Union, Washington, D.C., pp. 357-368.

Melchert, B., Devey, C.W., German, C.R., Lackschewitz, K.S., Seifert, R., Walter, M., Mertens, C., Yoerger, D.R., Baker, E.T., Paulick, H., Nakamura, K., 2008. First evidence for high-temperature off-axis venting of deep crustal/mantle heat: The Nibelungen hydrothermal field, southern Mid-Atlantic Ridge. Earth Planet. Sci. Lett. 275, 61-69.

Neal, C., Stanger, G., 1983. Hydrogen generation from mantle source rocks in Oman. Earth Planet. Sci. Lett. 66, 315-320.

Newman, K.R., Cormier, M.H., Weissel, J.K., Driscoll, N.W., Kastner, M., Solomon, E.A., Robertson, G., Hill, J.C., Singh, H., Camilli, R., Eustice, R., 2008. Active methane venting observed at giant pockmarks along the US mid-Atlantic shelf break. Earth Planet. Sci. Lett. 267, 341-352.

Proskurowski, G., Lilley, M.D., Kelley, D.S., Olson, E.J., 2006. Low temperature volatile production at the Lost City Hydrothermal Field, evidence from a hydrogen stable isotope geothermometer. Chem. Geol. 229, 331-343.

Proskurowski, G., Lilley, M.D., Seewald, J.S., Fruh-Green, G.L., Olson, E.J., Lupton, J.E., Sylva, S.P., Kelley, D.S., 2008. Abiogenic hydrocarbon production at Lost City hydrothermal field. Science 319, 604-607.

Resing, J.A., Baker, E.T., Lupton, J.E., Walker, S.L., Butterfield, D.A., Massoth, G.J., Nakamura, K.-i., 2009. Chemistry of hydrothermal plumes above submarine volcanoes of the Mariana Arc. Geochemistry, Geophysics, Geosystems 10, Q02009.

Schrenk, M.O., Kelley, D.S., Bolton, S.A., Baross, J.A., 2004. Low archaeal diversity linked to subseafloor geochemical processes at the Lost City Hydrothermal Field, Mid-Atlantic Ridge. Environmental Microbiology 6, 1086-1095.

Schwarzenbach, E.M., Lang, S.Q., Frah-Green, G.L., Lilley, M.D., Bemasconi, S.M., Mehay, S., 2013. Sources and cycling of carbon in continental, serpentinite-hosted alkaline springs in the Voltri Massif, Italy. Lithos 177, 226-244.

Stranne, C., Sohn, R.A., Liljebladh, B., Nakamura, K.I., 2010. Analysis and modeling of hydrothermal plume data acquired from the 85 E segment of the Gakkel Ridge. J. Geophys. Res.-Oceans 115. C06028, doi:10.1029/2009JC005776

Szponar, N., Brazelton, W.J., Schrenk, M.O., Bower, D.M., Steele, A., Morrill, P.L., 2013. Geochemistry of a continental site of serpentinization, the Tablelands Ophiolite, Gros Morne National Park: A Mars analogue. Icarus 224, 286-296.

Yoerger, D., Jakuba, M., Bradley, A., Bingham, B., 2007. Techniques for Deep Sea Near Bottom Survey Using an Autonomous Underwater Vehicle, in: Thrun, S., Brooks, R., Durrant-Whyte, H. (Eds.), Robotics Research. Springer Berlin Heidelberg, pp. 416-429.

Young, C., Lupton, J., 1983. An ultratight fluid sampling system using cold-welded copper tubing. Eos Trans. AGU 64, 735.

Appendix: Tikhonov Regularization of Eh Data

The Eh sensor measures the potential (in Volts) between a platinum electrode and a silver-silver chloride reference electrode sealed in a saturated KCl solution and connected to seawater through a porous liquid junction. Reduced hydrothermal species at the sensor surface induce a drop in potential across the electrodes (Resing et al., 2009) such that hydrothermal plumes manifest as negative deflections in sensor voltage. However, the use of the Eh sensor on a moving platform under heterogeneous conditions prevents full equilibration with any given fluid parcel, resulting in drift and hysteresis effects that preclude comparison of absolute voltages between casts and even within a single cast. We can mitigate the impact of a shifting baseline by computing the derivative of voltage with respect to time (dV/dt) over very short time scales (12 s for this study), such that the rapid change in voltage - characteristic of a plume-associated anomaly - appears as a negative peak in the time derivative.

While using a differentiated form of the data signal enables comparison of Eh anomalies between casts and between different depths of the same cast, the calculation amplifies sensor noise, thereby obscuring the plume signal. Smoothing the data before differentiating reduces sensor noise (e.g., Garcia, 2010), but also distorts or eliminates the rapid changes that constitute the signal of interest. To filter the noise in a non-destructive way, we turn to Tikhonov regularization, an approach to noise reduction specifically designed for noisy data with sharp, discontinuous features. This method has been applied to problems ranging from enhancing satellite imagery (Hansen, 2006) to interpreting electrocardiography measurements (Jiang, 2010). For this study, we use the implementation of Chartrand (2011), which applies explicitly to numerical derivatives.

Regularization theory is described in great detail elsewhere (Hansen et al., 2006; Hansen, 2010), so we provide only a brief description here with representative figures from a single cast to demonstrate the effect of regularization on this particular dataset. The differentiated Eh profile for any given cast is computed as the vector, u, that minimizes the following function (Chartrand, 2011):

$$F(u) = \alpha \int_0^L |u'| + \frac{1}{2}\int_0^L |Au - f|^2 \qquad (3)$$

where f is the original Eh voltage data (Fig. A-1A), u is the differentiated voltage after regularization (Fig. A-1B), A is anti-differentiation operator (such that Au represents the original data without noise), L is the length of the data vector, and α is the regularization parameter. The vector, u, that minimizes $F(u)$ represents the optimal balance between irregularity in the differentiated data (penalized by the first term on the right hand side) and deviation from the original data (penalized by the second term on the right hand side). Results of the analysis are shown in Fig. A-1B, in which some of the larger positive values (indicating recovery from a

plume-driven anomaly) are truncated to focus on the negative anomalies associated with a plume environment.

As *F(u)* can be minimized for any given α, it is important to choose this value carefully. To make this choice, we vary α over several orders of magnitude, and for each α, compute the norm of the solution, $\|u\|$, and the norm of the difference between the original data and reconstructed data, $\|Au - f\|$. For data that meet certain conditions (Hansen, 2010), a plot of $\ln\|u\|$ against $\ln\|Au - f\|$ takes the shape of an L (Fig. A-1C). Since these terms vary with α, the corner of the so-called L-curve gives the value for α that most effectively reduces noise without overly distorting the data. The corner point can be quantitatively identified with the Minimum Product criterion (Johnston and Gulrajani, 2000), which states simply that the corner lies where $\|u\|^2\|Au - f\|^2$ is at a minimum (Fig. A-1D). The value was calculated this way for each cast, and the results are tabulated in Table 2. Data fidelity for the chosen α can be assessed by comparing the reconstructed time series to the original time series data (Fig. A-1A), and we see that for our example cast, it is quite good. A bit of signal is smoothed out in the reconstructed data at ~700 m, but the much larger plume signal below 800 m is much more pronounced in the regularized derivative than in the unregularized derivative, where it is nearly washed out (Fig. A-1B). Data fidelity for all other casts in this study was generally as good as or better than for the example cast. The regularized derivative is identified with the nomenclature "$dEh/dt_{TR.}$"

The final step in processing the Eh data is to correlate gas data from discrete samples with the appropriate portion of the continuous dEh/dt_{TR} profile. For this correlation, we take the negative-most time derivative observed at station depth to best represent the reducing strength of the plume at that depth (following the method of Stranne et al., 2010). We use depth as the unifying parameter rather than time because down-casts give the most reliable sensor profiles, but samples were taken during up-casts. For matching sample bottles to time derivatives, we look within ±5 m of the sample location, which represents the smallest sample interval of the complete sample set. For the background profile (Cast #5), we match sample depths from Cast 1 to the dEh/dt_{TR} profile for cast 5 (located in the same spot as #1, but taken a few days later) because of the improved sensor stability compared to the first cast. Since the time derivative for background cast #5 is ~0 throughout, this approach has no impact on the shape of the profile. Even for non-background casts, the discretization of Eh time derivatives (shown in Fig. A-1B for our sample cast) does not change the nature of the continuous profiles, but merely allows us to get the most representative 'sample' of dEh/dt_{TR}. With this method, we observe a significant improvement in the correlation between redox potential and CH_4 concentration. A line fit to dEh/dt vs. CH_4 prior to regularization gives an r^2 of 0.25. After regularization, r^2 increases to 0.46, nearly double the value for unregularized dEh/dt data. Results for all samples are shown in Table 2. We note that, while this technique does an excellent job of noise reduction for a derived parameter, it is not a substitute for the calibration of individual sensor response with respect to

various reducing species, but it does establish a framework that could permit such a calibration in the future.

Figure Captions

Table 1. Cast locations in both longitude-latitude and local X-Y Cartesian coordinates. Alpha (α) values refer to the Tikhonov regularization parameter applied to each cast to compute dEh/dt_{TR} (Figs. 3A, 4A) as described in the appendix.

Table 2. Dissolved volatile data and corresponding dEh/dt_{TR} values at depths when sample bottles were fired. Error in ^3He is ~1%. Error in H_2, and CH_4 is ~2%. See appendix for discussion of dEh/dt_{TR}.

Table 3. Depths and H_2/CH_4 ratios of identified Lost City vents and the strongest water column plume signals. Rows are sorted by increasing depth such that water column anomalies on the right side of the table can only be explained by vent sources (left side) that are lower down in the table.

Figure 1. Schematic sketch of the distribution of venting chimneys from the Lost City field with gas concentrations in mmol/kg (sketch modified from Lang et al., 2012; gas data from Proskurowski et al., 2006, 2010). The field rests on a down-dropped terrace and the top of the massif (labeled 'cap') is capped by a ~1 m thick layer of carbonate ooze that has been hydrothermally cemented (Kelley et al., 2001; 2005; Blackman et al., 2002; Früh-Green et al., 2003; Karson et al., 2006).

Figure 2. Aerial view of the hydrocast locations over the main venting area. The color bar on the right shows depth in meters. The cast number for each marker is referenced in the legend. Hollow black diamonds show marked locations of venting. The dashed lines represent the Y-coordinate used for the two bathymetric profiles shown in the 2D cross sections (Fig. 4). These lines bracket the average Y-position of the casts used in creating the contours. The northern dashed line goes through the field's saddle point (shown in solid black in Fig. 4), representing the lower bathymetric bound for the area; the southern line crosses the main vent cluster, approximating an upper bathymetric bound. Backdrop bathymetry is courtesy of D. Kelley via http://www.lostcity.washington.edu/

Figure 3. Depth profiles collected during hydrocast survey of (A) potential temperature, (B) turbidity, (C) conductivity, (D) oxygen, (E) dEh/dt_{TR} (F) CH_4 (G) $^3He^{\Delta}$, and (H) H_2. Numbers in the legend shown in panel (B) refer to hydrocast identification number and apply to all panels in the figure. The marker styles in the legend in panel F apply to panels E-H whose profiles are based on discrete samples (cast numbering in this legend is the same as in panel B). The hydrothermal plume is not evident in 4 of the 5 sensors: conductivity, temperature,

transmissmometry, and dissolved oxygen (panels A-D). The time derivative of the Eh sensor, (Fig. 3E) shows a strong signal between 700 and 850 m that corresponds with elevated concentrations of H_2, CH_4 and $^3He^{\Delta}$ (panels F-H). Plumes that present as elevations in dissolved gas without concomitant changes in other properties represent a different style of venting than black smoker style plumes prevalent on axial MOR systems.

Figure 4. Two-dimensional cross-section of (A) dEh/dt_{TR}, (B) CH_4, (C) $^3He^{\Delta}$ and (D) H_2 generated from all non-background casts, with x-coordinates of known vents marked along the x-axis for reference. H_2 and CH_4 are shown in nM, dEh/dt in mV/s, and $^3He^{\Delta}$ in fmol/kg deviation from background. White dots represent sample locations. The vent cluster and Chaff Beach conspire to form a bi-layer plume with significant amounts of H_2 measured in casts conducted over Chaff Beach where there is no apparent focused flow. Solid black shape represents the bathymetry through the saddle point, and the black line represents the bathymetry through the vent cluster as described in the Fig. 2 caption.

Figure 5. Concentrations of H_2 vs. CH_4, normalized to the $^3He^{\Delta}$ content of the fluids. Only samples with $^3He^{\Delta}$ above 0.03 (the minimum statistically significant elevation) are plotted. Vent fluid data in green diamonds (from Proskurowski et al., 2006) and plume data (this work) in black circles. For comparison, the same data from other representative hydrothermal systems are also plotted including high temperature ultramafic systems on the Mid-Atlantic Ridge (includes Rainbow, Logatchev1 and Drachenschlund), Mid-Atlantic Ridge Hot Spots (includes Lucky Strike and Menez Gwen), basalt hosted systems on the Mid-Atlantic Ridge (includes Snake Pit and TAG) and basalt hosted systems in the Pacific Ocean (includes Southern Juan de Fuca, EPR 21˚N, EPR 13˚N, EPR 9˚50'N). Data from Keir et al. (2010) and Charlou et al.(2010) and references therein.

Figure 6. Percent difference (loss) of $H_2/^3He^{\Delta}$ vs $CH_4/^3He^{\Delta}$ from highest measured values of endmember vent fluids. Only samples with $^3He^{\Delta}$ above 0.03 are plotted. Vent fluids collected in GasTight samplers in diamonds (data from Proskurowski et al., 2006) and vent fluids collected by hydrocasts in black circles (this work). Movement from lower to higher percentages along the x-axis and y-axis indicates increasingly depleted CH_4 and H_2 concentrations, respectively, compared to end-member vent fluids.

Figure A-1. Panel plot showing the application of Tikhonov regularization to Cast #8. (A) The original profile is shown in blue with depth on the left y-axis and time on the right. The profile reconstructed from the regularized derivative is shown in red. (B) Time derivative of Eh (dEh/dt_{TR}) both before regularization (blue) and after (red). Black circles represent depths where samples were taken. Black squares show the negative-most time derivative within ±5 m of sample depth; these are tabulated for all casts in Table 2. (C) L-curve used to identify optimal Tikhonov regularization parameter, represented in the dimensional space of the L-curve by the

black box. (D) Minimum product plot used to quantitatively identify the optimal value for α based on the L-curve in part (C); this value is indicated by the black box.

Table 1.

Cast Number	Latitude (°N)	Longitude (°W)	X	Y	α
AT734V1	30 05.0000	42 08.0000	4822	5542	-
AT734V3	30 07.4352	42 07.2063	6100	10042	0.078
AT734V4	30 07.4340	42 07.2048	6100	10039	0.002
AT734V5	30 05.0000	42 08.0000	4822	5542	0.030
AT734V6	30 07.4346	42 07.2239	6080	10030	0.004
AT734V7	30 07.4613	42 07.2259	6070	10090	0.007
AT734V8	30 07.4346	42 07.2846	5970	10040	0.055
AT734V9	30 07.4290	42 07.1557	6180	10030	0.004
AT734V10	30 07.3590	42 07.4630	5685	9900	0.004
AT734V11	30 07.3407	42 07.7541	5520	9867	0.013
AT734V12	30 07.4289	42 07.2183	6080	10030	1.438
AT734V13	30 07.4679	42 07.2118	6090	10101	0.018
AT734V14	30 07.4501	42 07.1428	6200	10069	0.048

3 **Table 2.**

Cast ID	depth (m)	dEh/dt (mV/s)	^3He (fmol/kg)	$^3He^{\Delta}$ (fmol/kg)	H_2 (nM)	CH_4 (nM)
1	2500	0	2.64	0.00	2	1
1	2002	0	2.67	0.00	3	2
1	1501	0	2.70	0.00	2	1
1	1253	0	2.69	0.00	1	1
1	1002	-7	2.68	0.00	0	1
1	750	-22	2.61	0.00	3	2
1	501	0	2.43	0.00	1	3
3	719	-21	2.60	0.01	0	4
3	701	-21	2.60	0.03	1	2
3	650	-91	2.55	0.01	0	2
3	601	-3	2.51	0.01	0	2
3	550	-4	2.50	0.03	0	2
3	500	0	-	-	1	3
3	401	-9	2.41	-	0	2
4	747	-145	2.69	0.08	80	33
4	734	-44	2.65	0.05	19	8
4	651	-17	2.57	0.03	1	2
6	771	0	2.61	-0.01	14	2
6	750	-66	2.63	0.02	16	2
6	741	-1772	-	-	59	21
6	721	-1074	2.64	0.05	41	5
6	700	-28	2.60	0.03	5	2
6	649	0	2.57	0.03	3	2
6	601	0	2.53	0.03	3	2
6	500	0	2.43	0.00	1	3
7	794	-237	2.76	0.14	317	43
7	781	-134	2.75	0.13	51	8
8	751	-44	2.64	0.03	2	1
8	700	-197	2.62	0.05	1	2
8	601	-22	2.54	0.04	1	2
9	831	-1879	3.16	0.53	153	179
9	810	-120	2.76	0.14	26	29
9	780	-64	2.67	0.05	28	10
9	731	-43	2.59	0.00	3	2
9	650	-110	2.55	0.02	-	-
10	988	-12	2.65	-0.02	1	1
10	950	-7	2.66	-0.01	0	1
10	900	-13	-	-	0	1
10	751	-61	2.64	0.03	48	7
10	701	0	2.55	-0.02	0	2
11	1004	-3	2.66	-0.02	1	1
11	950	0	2.66	0.00	1	1
11	801	1	-	-	5	3
12	771	-21	-	-	27	8
12	750	-10	-	-	3	2
12	746	-6	-	-	5	3
12	726	0	-	-	0	1
12	701	0	-	-	0	1
13	791	0	-	-	9	8
13	776	-16	-	-	1	2
13	741	-623	-	-	156	54
13	736	-623	-	-	77	28
13	720	-2	-	-	2	2
13	701	-9	-	-	2	1

Cast ID	depth (m)	dEh/dt (mV/s)	^{3}He (fmol/kg)	$^{3}He^{\Delta}$ (fmol/kg)	H_2 (nM)	CH_4 (nM)
7	751	-54	2.63	0.02	349	53
7	701	-8	2.61	0.03	6	3
8	847	1	2.66	0.02	8	8
8	825	-148	2.70	0.07	28	18
8	800	-100	-	-	51	14

Cast ID	depth (m)	dEh/dt (mV/s)	^{3}He (fmol/kg)	$^{3}He^{\Delta}$ (fmol/kg)	H_2 (nM)	CH_4 (nM)
14	813	-9	-	-	30	6
14	800	-91	-	-	82	15
14	780	-29	-	-	293	47
14	700	-5	-	-	0	2

Table 3.

Vent Marker ID	Water Depth (m)	H_2/CH_4	CTD cast ID	Depth (m) of strongest signal	H_2/CH_4	Possible Source
Mk 3	730	8.8				
			6	741	2.8	BH/2/6/C/7
			13	741	2.9	BH/2/6/C/7
Mk BH	744	9.1				
			4	747	2.4	2/6/C/7
			10	751	6.9	out of field
			7upper	751	6.6	6/C
Mk 2	764	3.1				
			12	771	3.4	6/C/7
Mk 6	778	9.3				
			14	780	6.2	C
Mk C	780	10.1				
			7lower	794	7.4	Chaff Beach
			8	800	3.6	7
Mk 7	801	4.2				
Mk 8	802	2.3				
			9	831	0.9	H
Mk H	850	0.93				

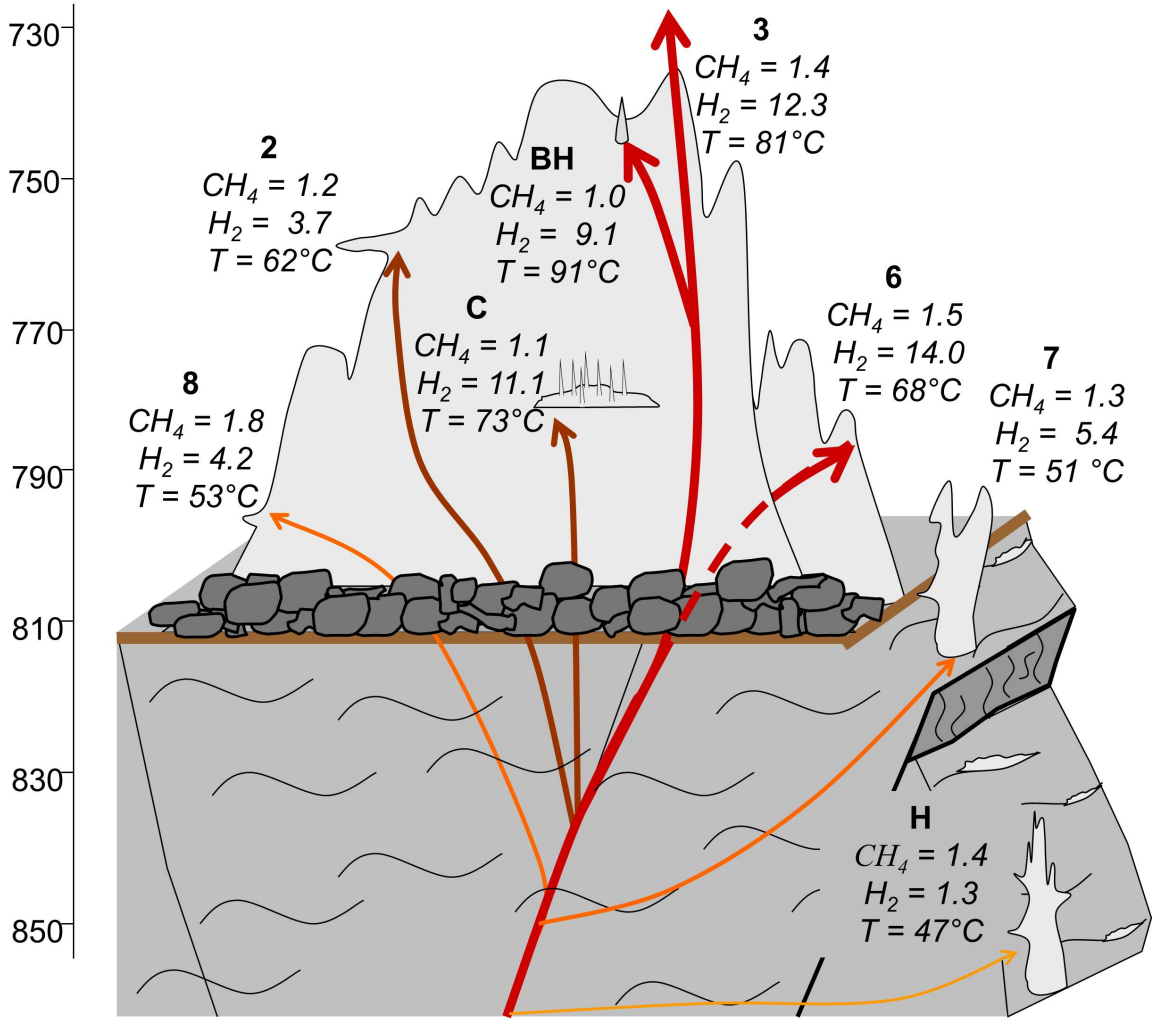
730
750
770
790
810
830
850
3
CH_4 = 1.4
H_2 = 12.3
T = 81°C
2
CH_4 = 1.2
H_2 = 3.7
T = 62°C
BH
CH_4 = 1.0
H_2 = 9.1
T = 91°C
C
CH_4 = 1.1
H_2 = 11.1
T = 73°C
6
CH_4 = 1.5
H_2 = 14.0
T = 68°C
7
CH_4 = 1.3
H_2 = 5.4
T = 51 °C
8
CH_4 = 1.8
H_2 = 4.2
T = 53°C
H
CH_4 = 1.4
H_2 = 1.3
T = 47°C

Figure 1.

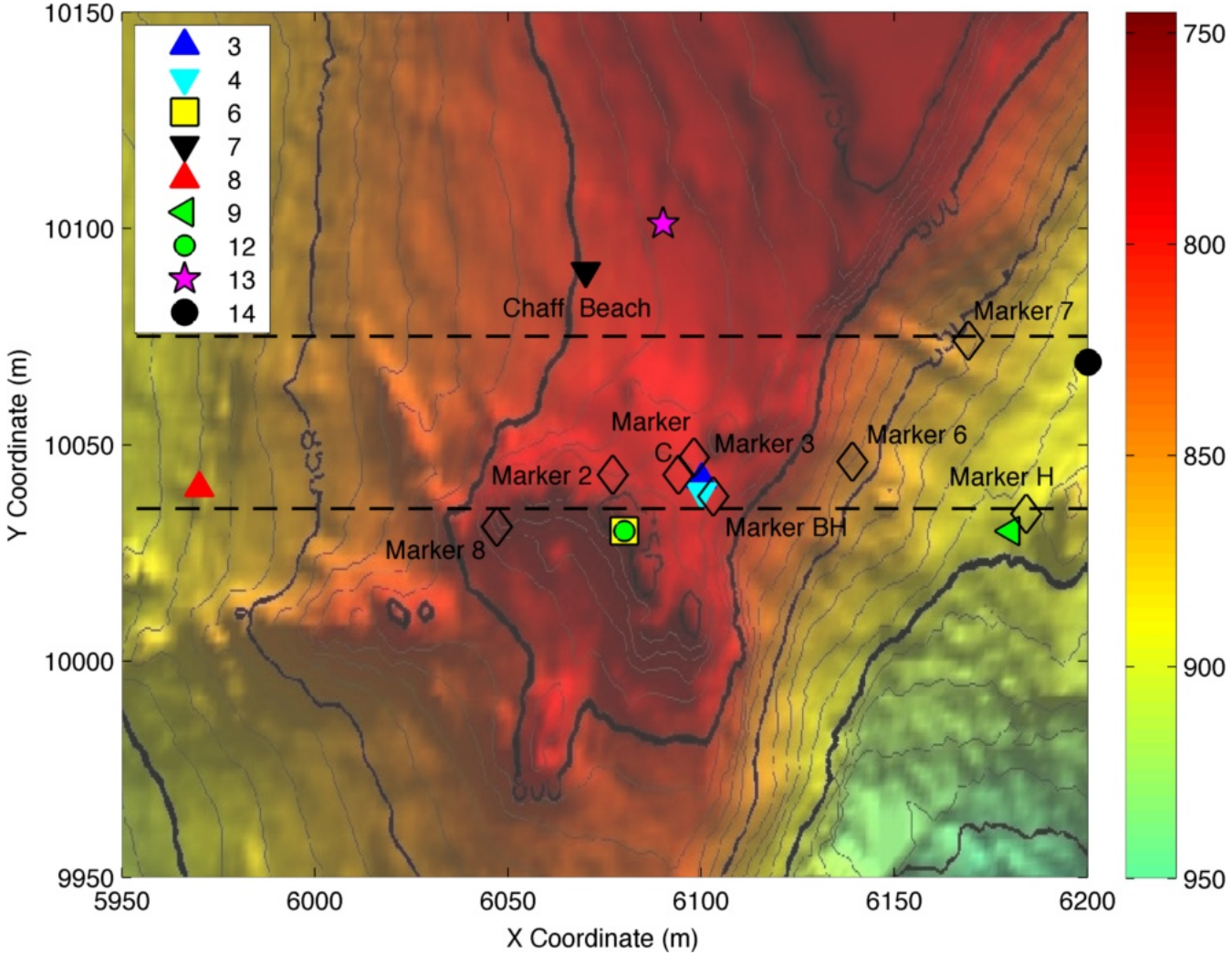
3
4
6
7
8
9
12
13
14
Chaff Beach
Marker 7
Marker C
Marker 3
Marker 6
Marker 2
Marker H
Marker BH
Marker 8
10150
10100
10050
10000
9950
5950
6000
6050
6100
6150
6200
750
800
850
900
950
Y Coordinate (m)
X Coordinate (m)

Figure 2.

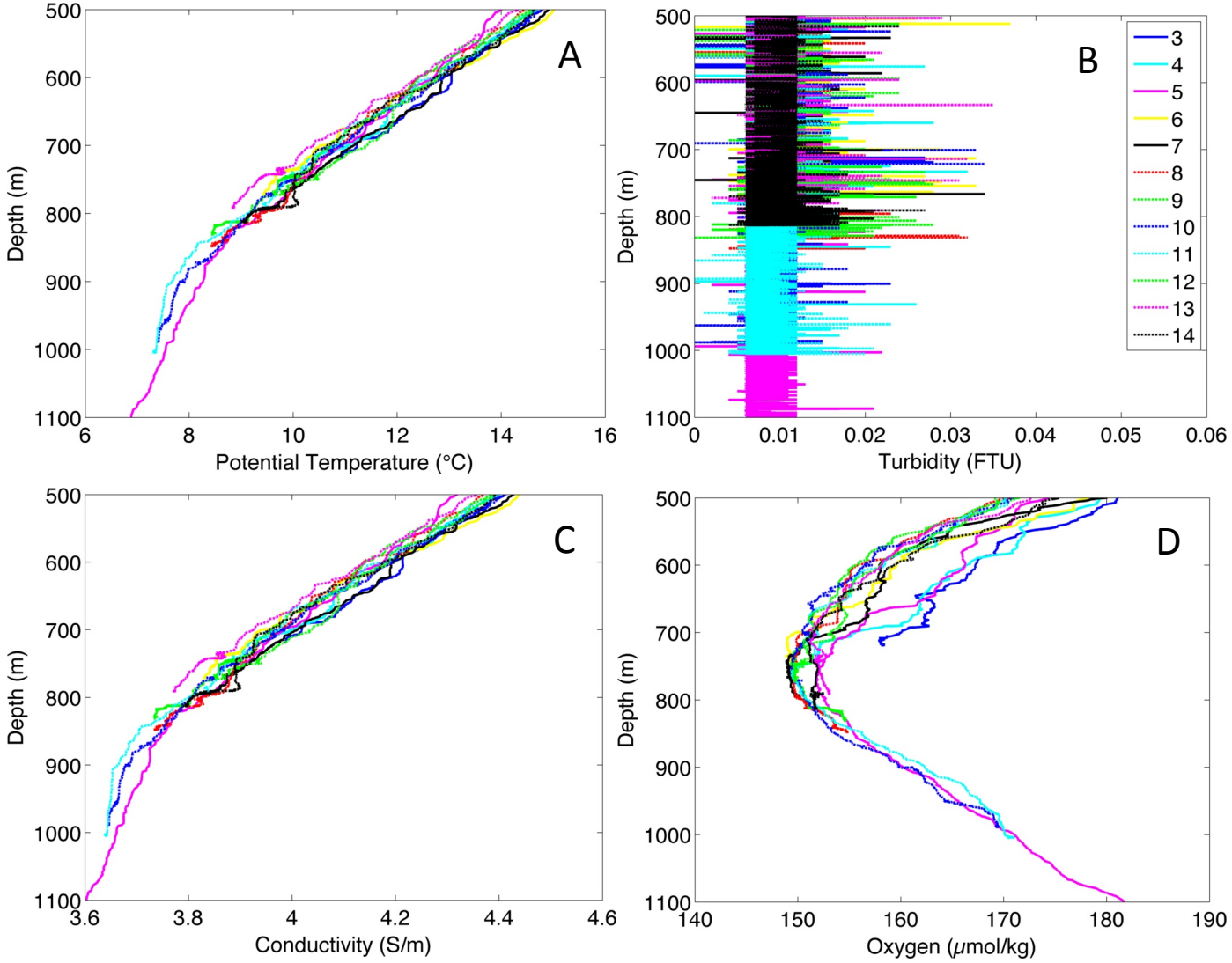
A
B
C
D
Depth (m)
Potential Temperature (°C)
Turbidity (FTU)
Conductivity (S/m)
Oxygen (μmol/kg)
3
4
5
6
7
8
9
10
11
12
13
14

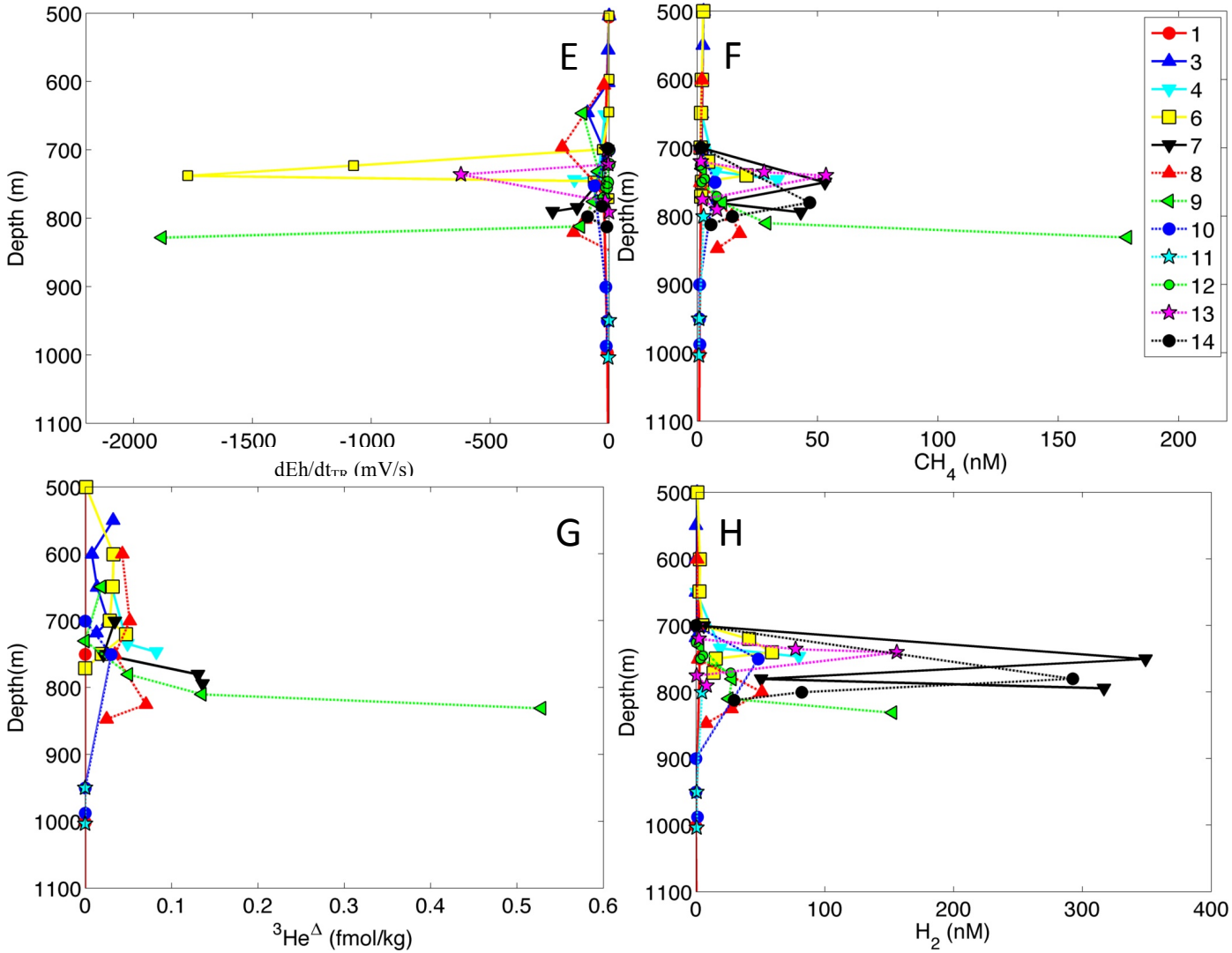
E
F
G
H
Depth (m)
Depth(m)
dEh/dt$_{TP}$ (mV/s)
CH$_4$ (nM)
^{3}He$^\Delta$ (fmol/kg)
H$_2$ (nM)
1
3
4
6
7
8
9
10
11
12
13
14

Figure 3.

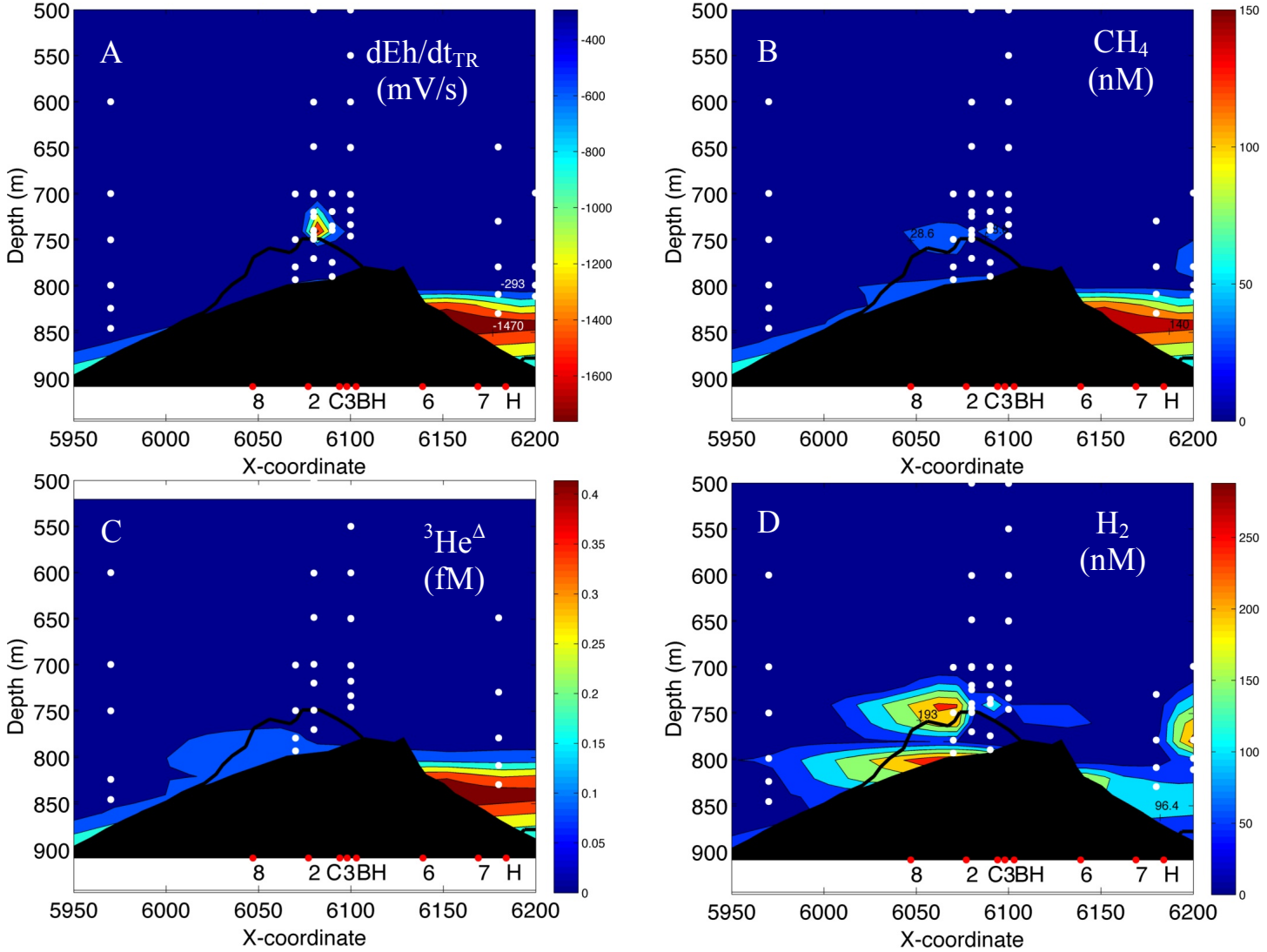
A
dEh/dt$_{TR}$
(mV/s)
B
CH$_4$
(nM)
C
^{3}He$^\Delta$
(fM)
D
H$_2$
(nM)
Depth (m)
X-coordinate
8
2 C3BH
6
7
H
-293
-1470
28.6
140
193
96.4

Figure 4.

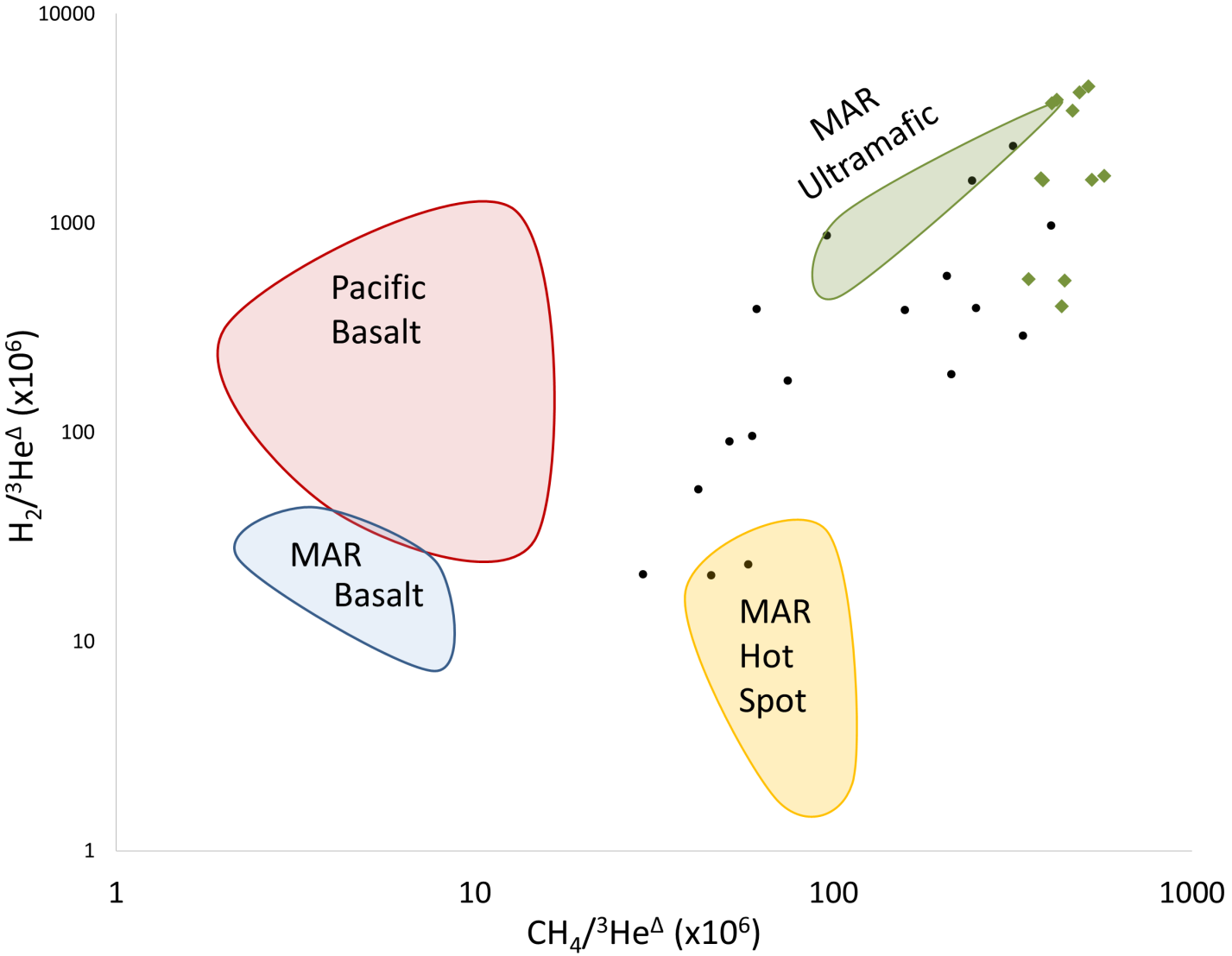
10000
1000
100
10
1
$H_2/^3He^\Delta$ (x10^6)
1
10
100
1000
$CH_4/^3He^\Delta$ (x10^6)
Pacific
Basalt
MAR
Basalt
MAR
Ultramafic
MAR
Hot
Spot

Figure 5.

Figure 6.

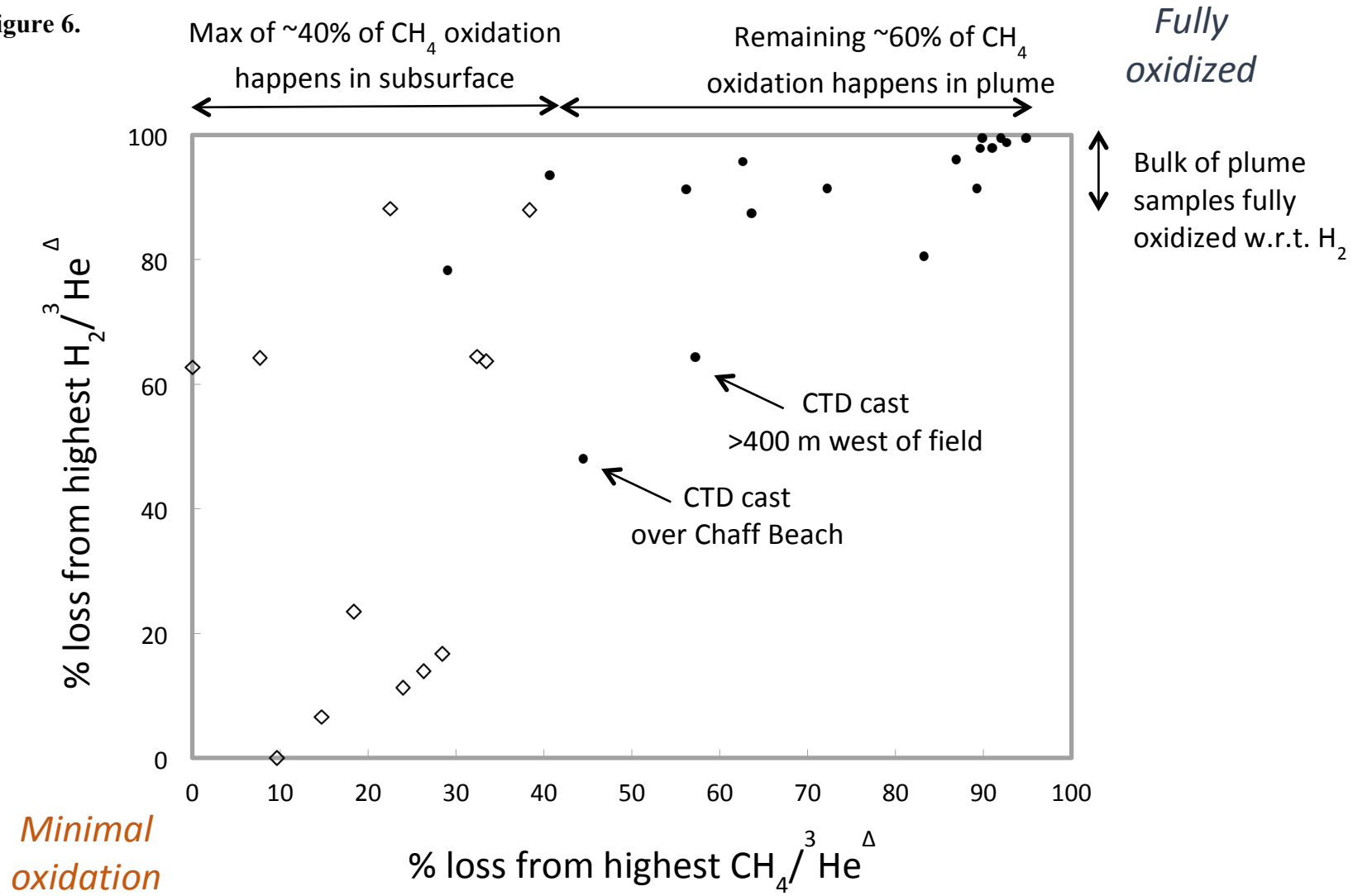
Max of ~40% of CH4 oxidation happens in subsurface
Remaining ~60% of CH4 oxidation happens in plume
Fully oxidized
Bulk of plume samples fully oxidized w.r.t. H2
CTD cast >400 m west of field
CTD cast over Chaff Beach
Minimal oxidation
% loss from highest H2/3He Δ
% loss from highest CH4/3He Δ
0
20
40
60
80
100
0
10
20
30
40
50
60
70
80
90
100

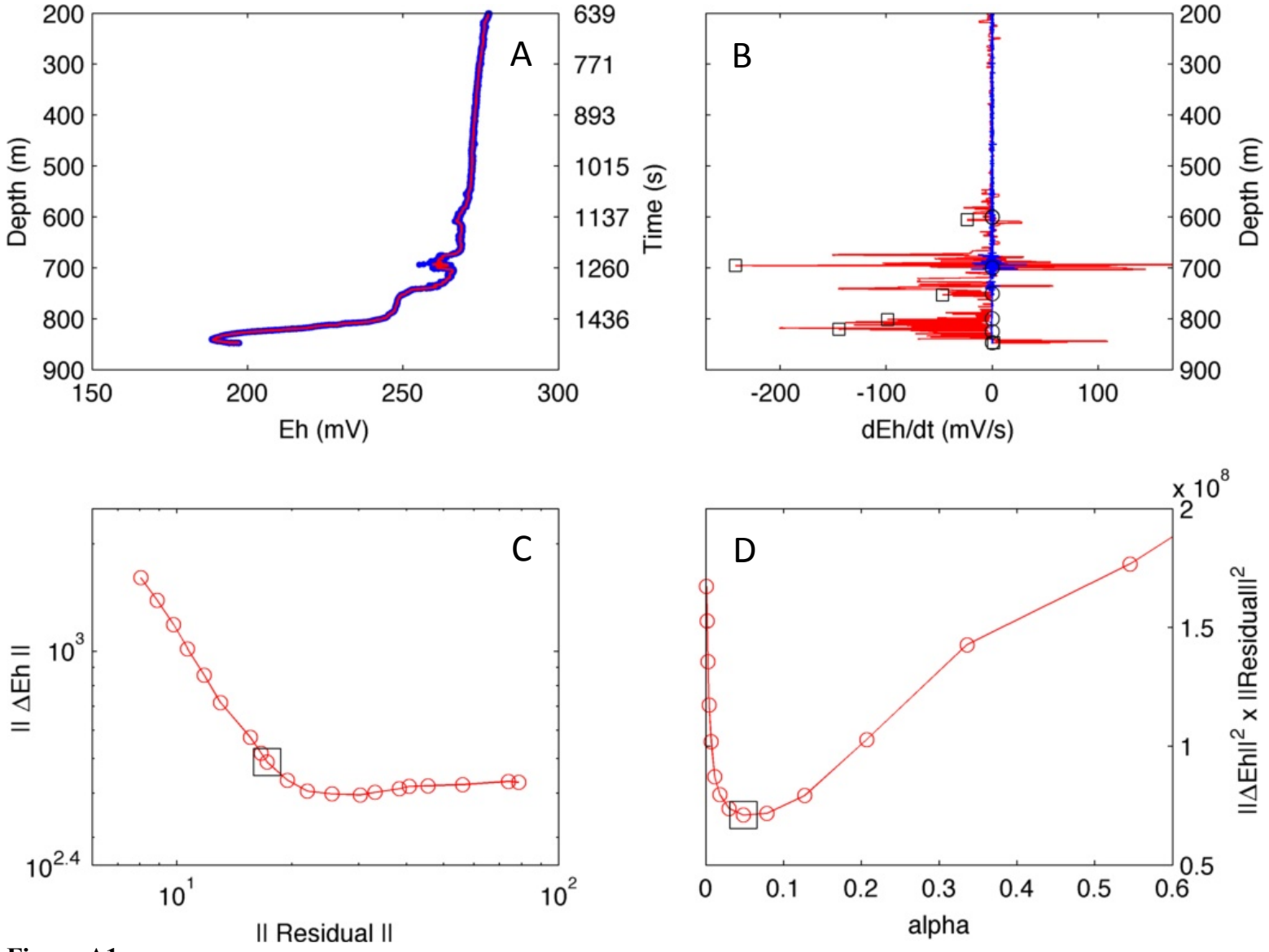
A
B
C
D
Depth (m)
Time (s)
Eh (mV)
dEh/dt (mV/s)
|| ΔEh ||
|| Residual ||
alpha
x 10^8
||ΔEh||^2 x ||Residual||^2

Figure A1.